Leveraging Intramolecular π-Stacking to Access an Exceptionally Long-Lived ^{3}MC Excited State in an Fe(II) Carbene Complex

Robert J. Ortiz,[a] Rajarshi Mondal, [a] James K. McCusker,[b] and David E. Herbert*[a]*

[a] Department of Chemistry and the Manitoba Institute for Materials, University of Manitoba, 144 Dysart Road, Winnipeg, Manitoba, R3T 2N2, Canada; *david.herbert@umanitoba.ca

[b] Department of Chemistry, Michigan State University, East Lansing, Michigan, 48824, USA; *jkm@chemistry.msu.edu

ABSTRACT

The ability to manipulate excited state decay cascades using molecular structure is essential to the application of abundant-metal photosensitizers and chromophores. Ligand design has yielded some spectacular results elongating charge-transfer excited state lifetimes of Fe(II) coordination complexes, but triplet metal-centered (^{3}MC) excited states—recently demonstrated to be critical to the photoactivity of isoelectronic Co(III) polypyridyls—have to date remained elusive, with temporally isolable examples limited to the picosecond regime. With this report, we show how strong-field donors and intramolecular π-stacking can conspire to stabilize a long-lived ^{3}MC excited state for a remarkable 4.1 ± 0.3 nanoseconds (ns) in fluid solution at ambient temperature. Analysis of variable-temperature time-resolved absorption data using theoretical approaches ranging from a simple Arrhenius model to semi-classical Marcus theory, combined with computational modelling and X-ray crystallography, reveal a Jahn-Teller stabilized excited state with a high activation barrier for ground-state recovery. The net result is a chromophore with a ^{3}MC excited-state lifetime that is orders of magnitude longer than anything yet observed for an Fe(II) complex.

INTRODUCTION

Harnessing sunlight to drive photophysical processes and chemical reactivity is a long-standing goal in science,[1] one made ever more urgent by the need to improve sustainability in energy harvesting and chemical synthesis.[2,3] Transition metal coordination complexes are a particularly attractive class of chromophores for virtually all such applications, thanks to synthetically tunable electronic structures and a predilection for absorbing visible light to generate long-lived, charge-separated excited states whose chemical potential can be leveraged for photo-induced electron transfer.[4] Historically, the applied photochemistry of coordination complexes has been dominated by second- (4*d*) and third-row (5*d*) transition metals as a consequence of their strong ligand fields. These result in the relative stabilization of charge-transfer states (*e.g.*, metal-to-ligand charge transfer, MLCT; ligand-to-metal charge transfer, LMCT; inter/intra-ligand charge transfer, ILCT) compared to metal-centered (ligand-field) excited states.[5] Concerns over scarcity and how such elements are sourced,[6] however, is driving the push towards replicating these molecules' favorable photophysical properties in complexes based on more abundant metals.[7,8]

In the context of the privileged class of pseudo-octahedral d^6 complexes, exciting strides have been made replicating the CT-driven photochemistry of heavier analogues with first-row transition metals such as Cr(0)[9–11] and Mn(I).[12,13] These significant advances notwithstanding, an argument can be made for leveraging ligand-field excited states in the pursuit of abundant-element photochemistry.[14] Metal-centered (MC) excited states which are responsible for the rapid deactivation of CT excited-states in iron polypyridyls, for example,[15] can also be photochemically active. Notably, photogenerated high-spin Fe(II) has been shown to engage in electron transfer chemistry from a quintet metal-centered $^5T_2$ excited state[16] and recent work has demonstrated how triplet metal-centered $^3T_1$ excited states (S = 1) of Co(III) complexes can be luminescent[17] and

efficiently mediate photocatalysis.[18,19] Beyond reactivity, controlling spin-states with light also boasts promise for quantum information science applications.[20] Accordingly, there is on-going vigorous interest in understanding how ligand design can be further exploited to manipulate the entirety of the excited state landscape of 3*d* coordination complexes.

While accessible for Co(III), the triplet metal-centered excited state (^{3}MC) has been elusive for isoelectronic Fe(II). The critical problem stems from a combination of the lifetime and nature of the lowest-energy excited state typically found for such compounds. Archetypal excited-state evolution from the initially formed MLCT state to the lowest-energy excited state in iron chromophores involves ^{3}MC states as part of a cascade sequence (Figure 1a), ultimately resulting in the formation of a ^{5}MC state (specifically, the $^5T_2$ state).[21] While the ^{5}MC excited state can persist for nanoseconds or longer,[22] it is relatively low in energy: this limits its potential for applications in light-to-energy conversion schemes. The higher-lying triplet state, on the other hand, is more energetic and is characterized by a smaller geometric distortion but suffers from a very short lifetime: even 'longer-lived' examples persist only on the timescale of tens of ps,[23–25] with one recent example extending to 63 ps.[26] In $[Fe(bpy)_3]^{2+}$ (bpy = 2,2'-bipyridyl), the build-up of the relatively long-lived ^{5}MC lowest energy excited state (*ca.* 1 ns) is complete within a couple of hundred femtoseconds; the intermediate ^{3}MC state never achieves any sort of quasi-steady-state population, as its lifetime of 70 ± 30 fs is faster than its inferred time constant for formation (150 ± 50 fs).[27] The origin of this rapid decay, as with the origin of the short CT lifetimes of 3*d* complexes in general, stems from the relative energetics of these various excited states.[15] In the absence of competing factors, the lower ligand field strength of the 3*d* transition metals results in an energetic ordering mirroring the aforementioned deactivation pathway. Each lower energy MC state intersects the next higher energy state close to its energetic minimum, resulting in an

essentially barrierless, ballistic state-to-state conversion process that facilitates rapid non-radiative decay to the lowest-energy excited state of the compound.

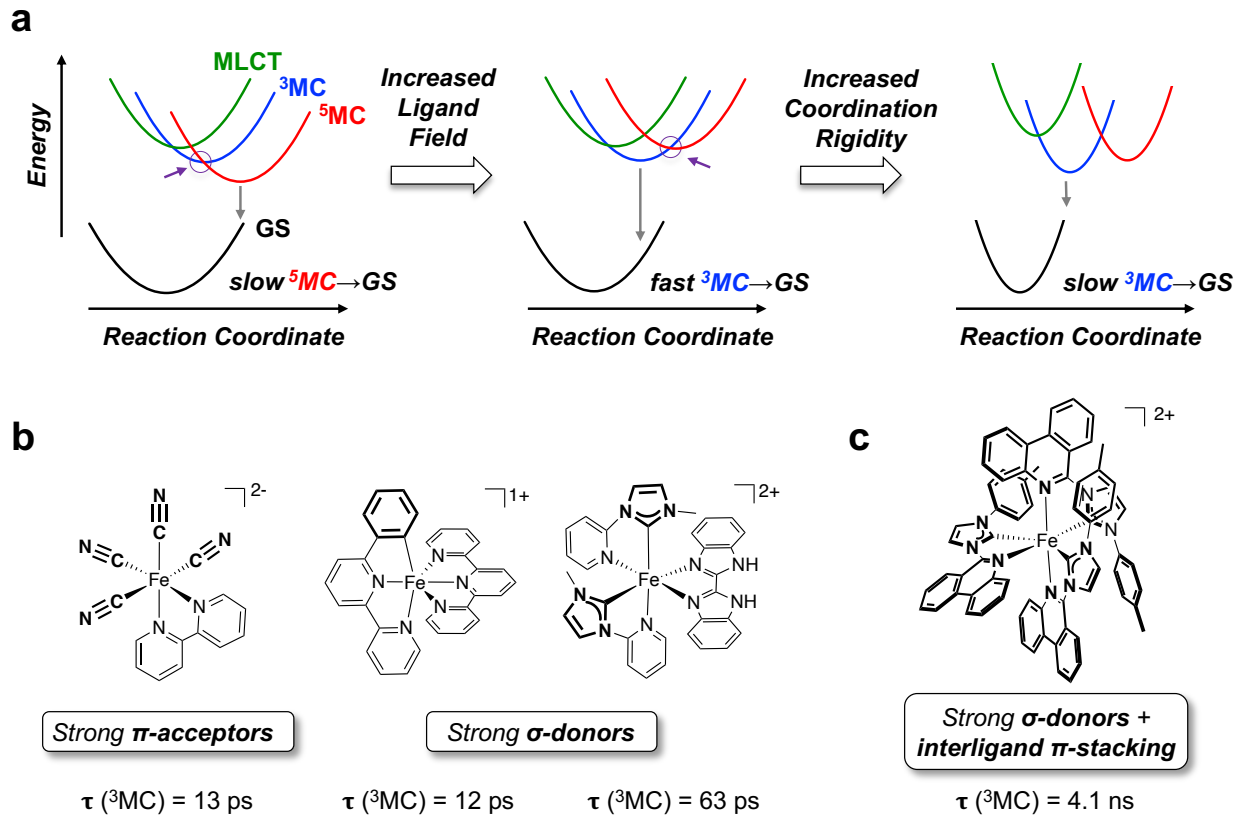

Figure 1. *(a) Potential energy surfaces typical of low-spin pseudo-octahedral d^6 Fe(II) with the ^{3}MC/^{5}MC minimum energy crossing point circled. The "reaction coordinate" refers to whichever (combination of) normal vibrational mode(s) is coupled to the spin-state interconversion. The typically 'slower' (~ ns) relaxation of ^{5}MC excited states arises from the $\Delta S = 2$ difference in spin multiplicities and the need for a second-order spin−orbit interaction through the intermediacy of a ^{3}MC state. For destabilized ^{3}MC excited states operating in the Marcus normal region (central diagram), the increased excited-state energy accompanying a stronger ligand field leads to shorter lifetimes for ground-state recovery. (b) Examples of Fe(II) species exhibiting 'long-lived' ^{3}MC excited states;[24–26] (c) The approach reflected in this report, which combines strong σ-donation from the ligand with intramolecular ligand-ligand interactions that serve to rigidify the structure, leading to a significantly torsionally distorted quintet excited state. Coupled with a Jahn-Teller distorted and stabilized ^{3}MC excited state, this decreases the rate of non-radiative decay back to the ground state.*

As with CT excited states, accessing longer-lived transient ^{3}MC states therefore requires reordering these excited states by overcoming the dampened ligand field strength of first-row transition metals that arises from attenuated metal-ligand orbital overlap caused by contracted 3*d* orbitals.[15] The most prominent strategy used to date to lengthen MLCT excited state lifetimes is to employ increasingly strong field ligands such as cyanide,[28–32] cyclometalated ligands,[33,34] or carbenes.[35–37] Depending on the ligand, there should ostensibly be a differential impact on the MLCT, ^{3}MC and ^{5}MC excited state energies for d^6 configurations. Strong π-acceptors such as cyanide should stabilize the ground state (with full occupancy of the π-symmetric t_{2g} orbitals) more so than the MLCT or ^{3}MC states (with five t_{2g} electrons), and more so still than the ^{5}MC state (with four t_{2g} electrons). Strong σ-donors should in turn destabilize the metal-ligand $\sigma_{antibonding}$ e_g^* orbitals and with them, destabilize the ^{5}MC excited state the most, followed by the ^{3}MC state. Balancing these effects has been implicated in the solvent control over excited-state relaxation pathways observed for Fe(II) cyanido complexes with mixed donor sets[24,38] in which ^{3}MC excited states can be lower in energy than strongly distorted ^{5}MC states. There is also by now extensive evidence that incorporating multiple carbene donors into the coordination sphere of Fe(II) reorders excited state energies such that the $^5T_2$ state is destabilized beyond the $^3T_1$.[23,39–44] Despite these impacts, lifetimes of temporally isolable ^{3}MC states for Fe(II) photosensitizers remain firmly ensconced in the ps regime (Figure 1b).[23–26]

With a lower oxidation state in a d^6 configuration, strong light absorption by pseudo-octahedral ferrous chromophores can typically be achieved in the mid-visible region of the spectrum, in contrast to the near-UV photons required for their Co(III) counterparts.[19] Combined with an unparalleled abundance in the transition series, such features make Fe a tantalizing target for sustainable chromophore design.[45] But to further push the boundaries of excited state

manipulation, new strategies are clearly required.[46] Here, we describe a novel approach leveraging the combined effect of inter-ligand π-stacking, strong-field carbene donors, and the heightened acceptor character of a benzannulated pyridine ligand, to access an exceptionally long-lived ^{3}MC excited state in an Fe(II) coordination complex (Figure 1c).

RESULTS AND DISCUSSION

Synthesis. Our prior work on the coordination properties of phenanthridine (benzo[*c*]quinoline) heterocycles[47] provided an entry point to a hybrid ligand combining strongly σ-donating carbene moieties and benzannulated donors that could also exhibit heightened inter-ligand π-stacking. The proclivity of phenanthridine-containing ligands to engage in *inter*molecular π-stacking has been implicated in the poor solubility of their square planar Pt(II) complexes, for example.[48] In addition, the 'imine-bridged biphenyl' character of the ground state of phenanthridines localizes the LUMO at the π*(C=N) sub-unit, proffering enhanced molecular rigidity to excited states of phenanthridine-containing coordination complexes.[49,50] Phenanthridine ligands also promote strong absorption of visible light, in particular in pseudo-octahedral Fe(II) complexes.[51] To further encourage inter-ligand interactions, we opted for tolyl {(4-methyl)phenyl)} substituents on the *N*-heterocyclic carbene fragment.

The target bidentate imidazolium ligand precursor was easily accessible via *N*-arylation of (*N*-tolyl)imidazole with 6-chlorophenanthridine.[52] At the elevated temperature of 170°C, both reactants are liquid and no solvent is required. The product solidifies out of the reaction mixture and counter-ion exchange gave the target salt [**L**H]PF_6 in a good isolated yield (78%; Figure 2a). [**L**H]PF_6 was comprehensively structurally characterized in solution and the solid-state, including via single-crystal X-ray diffraction analysis (Figure S1a). To form the Fe(II) complex, it is

necessary to first mix [**L**H]PF_6 with the ferrous precursor (here, $FeBr_2$) and then add an exogeneous base. Specifically, a THF solution of the ligand precursor salt and $FeBr_2$ was heated to reflux in THF for 16 hours, at which point the mixture was cooled to ambient temperature and an excess of KO*t*Bu introduced (Figure 2b). We note there is no conversion to product if the base is added first. The complex was isolated as a PF_6^- salt, with multiple recrystallizations performed yielding a spectroscopically pure, dark red crystalline product.

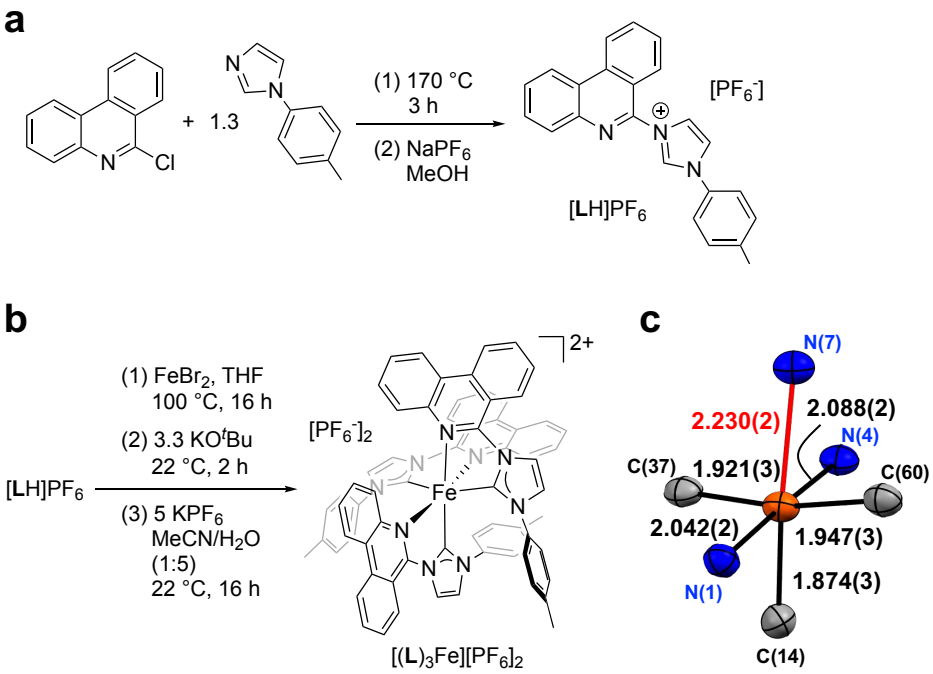

Figure 2. *Synthesis of (a) the ligand precursor [**L**H]PF_6 and (b) its ferrous complex [(**L**)$_3$Fe][PF_6]$_2$. The primary coordination sphere around Fe is highlighted in (c) with bond distances given in angstroms.*

Geometric and Electronic Structure. Facial vs. meridional selectivity in pseudo-octahedral Fe(II) complexes of hybrid carbene/*N*-heterocycle ligands has been previously noted to be a function of the steric demand of the azine moiety, with little influence from the steric constraints

of the carbene unit.[53] With pyridine donors, bulky mesityl substituents can promote formation of mixtures dominated by *mer* isomers but complexes of quinolinyl/carbene ligands almost exclusively form *fac* isomers (Table S1).[53] Here, multinuclear NMR spectroscopic analysis of $[(\mathbf{L})_3Fe][PF_6]_2$ in solution is consistent with the presence of a single isomer of low symmetry. Interestingly, diffraction from single crystals grown at ambient temperature from acetonitrile solutions layered with diethyl ether revealed a *mer* arrangement of the bidentate *C^N* ligands about the Fe(II) ion and a strongly distorted octahedral geometry enforced by substantial inter-ligand π-π interactions (Figure S1b). These distortions are much more pronounced in $[(\mathbf{L})_3Fe]^{2+}$ than in related Fe(II) carbene/*N*-heterocycle complexes, regardless of the stereochemistry at the metal (Table S2). The *trans* influence of the carbene donors is manifested in a particularly long Fe(1)-N(7) bond distance {2.230(2) Å, Figure 2c}; the two Fe-N distances involving phenanthridinyl donors *trans* to each other are much shorter {Fe(1)-N(1) 2.042(2) Å, Fe(1)-N(4) 2.088(2) Å} and in line with other pseudo-octahedral, low-spin Fe(II) complexes of phenanthridine-containing ligands.[54] The phenanthridinyl donor {N(7)} involved in the distinctly long Fe-N interaction is π-stacked with a second phenanthridinyl ring {N(4)}. Both exhibit substantially bent angles with respect to their coordination to Fe {$C_5N(4)$ centroid-N(4)-Fe(1) angle = 159°; $C_5N(7)$ centroid-N(7)-Fe(1) angle = 146°} compared with the third phenanthridinyl donor {$C_5N(1)$ centroid-N(1)-Fe(1) angle = 173°} which is sandwiched between two carbene tolyl substituents (Figure S2). These intramolecular π-π interactions persist in solution, evinced by broad peaks assigned to the ligand tolyl groups evident in the ^1H NMR spectrum slightly upfield of the usual aromatic region (5.8-6.8 ppm; Figure S3a) that sharpen upon heating (Figure S4). Similar spectroscopic features diagnostic of aromatic π-stacking have been reported in the protein NMR literature.[55] Here, peak broadening also appears in the $^{13}C\{^1H\}$ NMR (Figure S3b).

The steady-state solution absorption spectrum of $[(\mathbf{L})_3Fe]^{2+}$ is dominated by a broad, low energy peak centered at 500 nm (ε = 8 040 M^{-1} cm^{-1}, FWHM = 4580 cm^{-1}; Figure 3b and Figure S5). This absorption is nearly isoenergetic with that observed for a quinolinyl-carbene analog (508 nm),[53] a phenomenon we have noted before for phenanthridine/quinoline ligated metal complexes.[56] Minor solvatochromism is evident when switching from acetonitrile to tetrahydrofuran (Figure S6), consistent with the dipole-change expected of a MLCT-type transition.[57] Notwithstanding the aforementioned distortions from octahedral symmetry, density functional theory (DFT) calculations show the character of the three highest occupied molecular orbitals to be essentially that of the π-symmetric t_{2g}-like 3d orbitals of the metal (Figure 3a). At the ground-state geometry, metal-ligand σ* anti-bonding e_g-like character can be found in the LUMO+6 and LUMO+16 (Figure S7). The two most energetically accessible MOs are heavily localized on the phenanthridinyl fragments (LUMO, LUMO+1), in particular, at the π*(C=N) sub-unit (Table S4). Time-dependent DFT (TDDFT) simulations suggest this has strong interconfigurational character of MLCT-type, mainly involving the HOMO-1 and HOMO-2 which are best poised for overlap with the π*(C=N) moiety of one of the two phenanthridinyl ligand arms with bent coordination to the metal.

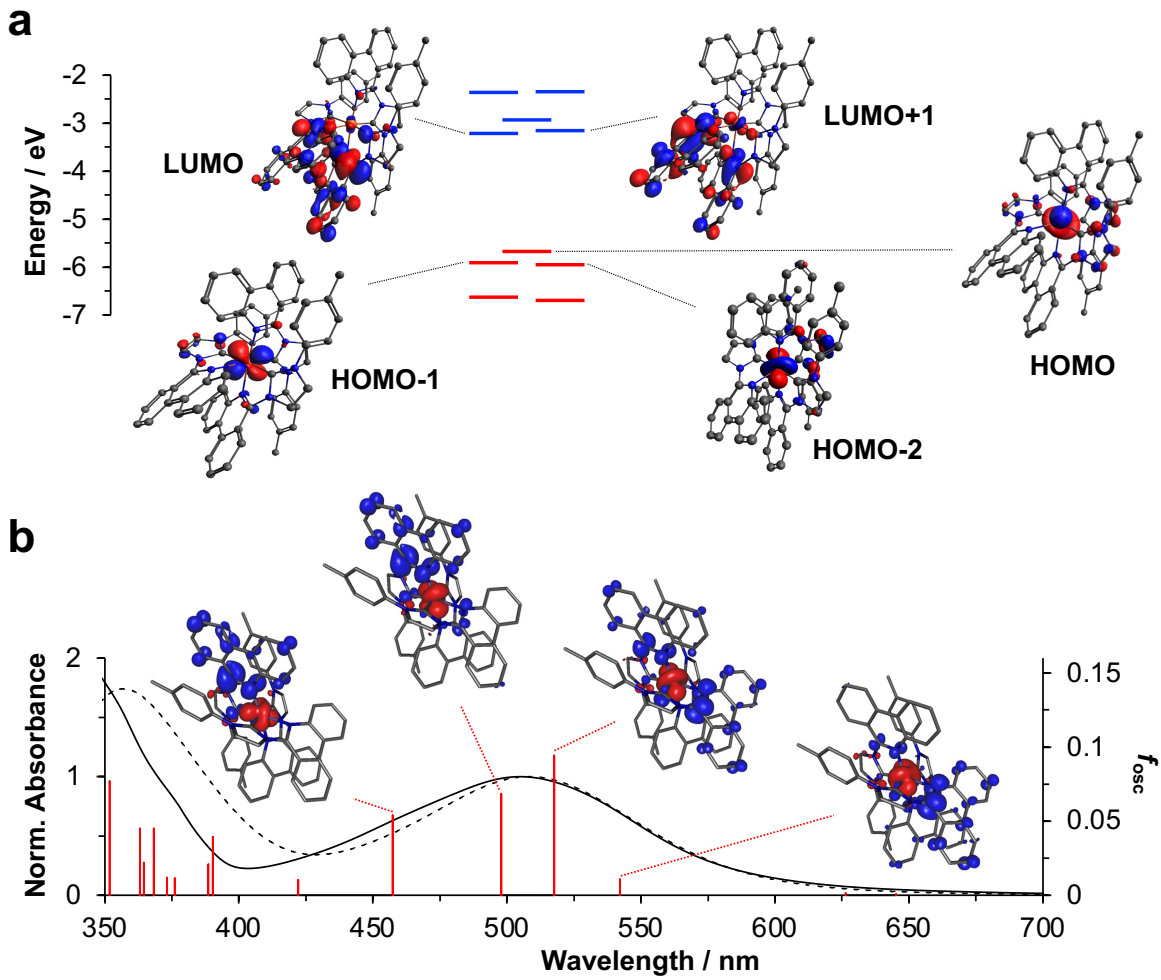

Figure 3. *(a) Frontier molecular orbitals for* $[(\mathbf{L})_3Fe]^{2+}$ *calculated in THF (isosurface value = 0.04); (b) Comparison of the experimental (-) with the computed (---) spectra, and vertical energy transitions (red solid line) for* $[(\mathbf{L})_3Fe]^{2+}$ *in THF (FWHM = 0.35 eV). At wavelengths below 600 nm all transitions are shown; at wavelengths above 600 nm only transitions with oscillator strengths greater than 0.01 are shown. Electron-hole density maps shown for four of the major lowest energy transitions (red = hole; blue = electron; isosurface value = 0.002).*

Consistent with the localization of the frontier orbitals, cyclic voltammetry shows a quasi-reversible metal-centered oxidation at + 0.52 V vs $FcH^{0/+}$ (FcH = ferrocene; Figure S8), supported by spectroelectrochemical data in which the MLCT absorption at ~500 nm is bleached on oxidation while a new broad, weak feature appears at ~850 nm consistent with LMCT involving Fe(III)

(Figure S9a). This oxidation is slightly more accessible than in complexes of pyridyl-[43] or quinolinyl-carbenes[53] but much less cathodically shifted than in hexa-carbene variants.[58] Also present in the electrochemistry is a well-resolved ligand-based reduction at -1.43 V. The absorption spectrum of the product of electrochemical reduction contains broad absorptions in the deep red (720 nm) and near IR (1000 nm) consistent with the presence of a benzannulated pyridinyl radical through the introduction of lower energy transitions (Figure S9b).[59] A second reduction is also accessible at -1.99 V which results in a bleaching of these new features (Figure S10).

Time-resolved Absorption Spectroscopy. Optical transient absorption (TA) spectroscopy at both short (fs) and long (ns) time delays were collected to interrogate the excited state dynamics of $[(\mathbf{L})_3Fe]^{2+}$. At early delay times (*i.e.*, < 1 ps), the difference spectra collected in THF following excitation at 480 nm resembles simulations of an MLCT excited state constructed from the spectroelectrochemically generated absorption spectra[60] of $[(\mathbf{L})_3Fe]^{+}$ and $[(\mathbf{L})_3Fe]^{3+}$ (Figure S11). This spectral profile evolves with a time constant of *ca.* 1 ps into one dominated by a bleach that spans much of the visible region (Figures S12 and S34). Excited state absorption features have been reported for ^{3}MC excited states in certain Fe(II) chromophores (Table S5), but the lack of any net absorptive features characteristic of a ligand radical anion is generally consistent with its assignment to a metal-centered (*i.e.*, ligand-field) excited state.[61] Single-wavelength kinetics monitored at 530 nm reveal ground-state recovery dynamics that can be fit to a single-exponential kinetic model with a time constant of 4.1 ± 0.3 ns (Figures S13 and S14).

At first blush, the photophysics of this compound appear relatively straightforward: an initially populated MLCT state decays into a MC state on the ps timescale, followed by ground-state recovery with a time constant of ~4 ns. Although phenomenologically this excited-state

cascade is similar to what has been documented for a number of Fe(II) polypyridyls,[62] these results are not as straightforward as they appear. First, the presence of three strong-field carbene donors in the coordination sphere of $[(\mathbf{L})_3Fe]^{2+}$ should present a significantly stronger ligand field toward Fe(II) relative to a compound such as $[Fe(bpy)_3]^{2+}$, for example. The photophysics of Fe(II) complexes are generally viewed as operating in the Marcus normal region:[23] given the expected increase in excited-state energy for $[(\mathbf{L})_3Fe]^{2+}$, this should lead to a larger rate constant (*i.e.*, shorter lifetime) for ground-state recovery. Yet the measured lifetime of $[(\mathbf{L})_3Fe]^{2+}$ is four-fold longer than the 1 ns lifetime of $[Fe(bpy)_3]^{2+}$ observed under identical experimental conditions. A similar conundrum was encountered when trying to understand the ground-state recovery kinetics of $[Co(bpy)_3]^{3+}$.[63] In that case, it was determined that the lowest energy excited state had switched from the $(t_{2g})^4(e_g)^2$-based $^5T_2$ state typical of Fe(II) to the $^3T_1$ state derived from a $(t_{2g})^5(e_g)^1$ excited-state configuration. There, the combination of increased zero-point energy and smaller reorganization energy pushes the Co(III) photophysics into the Marcus inverted region, explaining the increased lifetime. While a similar explanation might be plausible for $[(\mathbf{L})_3Fe]^{2+}$, decay cascades that have been identified for iron carbene-based chromophores where ^{3}MC excited states have been implicated in their ground-state recovery dynamics (*i.e.*, ^{3}MLCT $\rightarrow$ ^{3}MC $\rightarrow$ ^{1}GS) exhibit time constants that are orders of magnitude faster than what we have observed for $[(\mathbf{L})_3Fe]^{2+}$.[64,65] In this context, the 4 ns lifetime of the MC excited state of $[(\mathbf{L})_3Fe]^{2+}$ should be interpreted as abnormally long. Neither of these two scenarios thus appear to adequately explain our observations in any straightforward manner.

As we[63,66] and others[67,68] have shown, variable-temperature time-resolved absorption spectroscopy can be a powerful tool for extracting detailed information about ground-state recovery dynamics, particularly those involving ligand-field excited states of first-row metal

complexes. We therefore turned to this technique to further understand the highly unusual excited-state properties of $[(\mathbf{L})_3Fe]^{2+}$. The basic methodology that we employ for these measurements has been described in detail elsewhere;[63] specifics relevant to the data presented here can be found below in the Experimental Details section. Data were acquired for $[(\mathbf{L})_3Fe]^{2+}$ in both THF and acetonitrile solutions. The results obtained in both solvents are quite similar, so we will only discuss in detail the results in THF (the acetonitrile data can be found in the ESI). Single-wavelength kinetics for ground-state recovery were acquired at 460 nm following 480 nm excitation in a temperature range of 223-273 K in increments of 5 K (Figure 4), which were then combined with the aforementioned data point acquired at room temperature (*i.e.*, ~293 K). The data at each temperature were well described by a single-exponential kinetic model. The eight-fold increase in observed lifetime from 4.1 ± 0.3 ns at 292.5 K to 33.0 ± 0.8 ns at 223 K (Table S6) indicates the presence of a barrier that is significantly larger than what has been previously documented for either Fe(II) or Co(III) polypyridyl complexes.

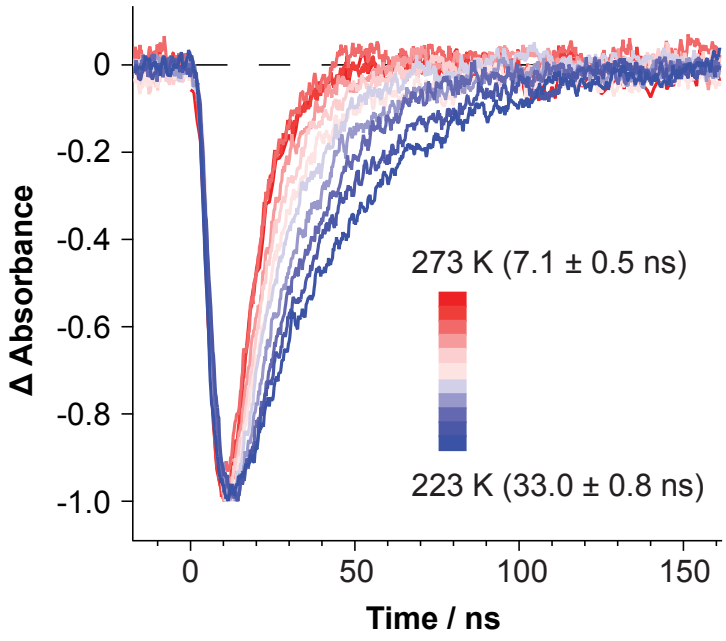

Figure 4. *Variable-temperature time-resolved absorption data acquired on* $[(\mathbf{L})_3Fe]^{2+}$ *in THF solution at* λ_{probe} *= 460 nm following excitation at* λ_{pump} *= 480 nm.*

The variable-temperature data were analyzed following the protocol employed to establish the origin of Marcus inverted region behavior in the excited-state dynamics of isoelectronic Co(III) polypyridyls[63] (see Supporting Information for a full description). In brief, we use three different theoretical constructs – (1) an Arrhenius model, (2) transition state theory (*i.e.*, the Eyring equation), and (3) semi-classical Marcus theory – to interpret the potential energy landscape that defines the excited-state dynamics of $[(\mathbf{L})_3Fe]^{2+}$. The Arrhenius model is the simplest of the three, parameterizing the variable-temperature data in terms of a Boltzmann distribution involving a barrier (E_a) and a so-called frequency factor (A) that corresponds to the rate of the process in the barrierless limit. As expected, a plot of $\ln(k_{obs})$ for ground-state recovery versus T^{-1} (where $k_{obs} = k_{nr}$ due to the absence of emission from the excited state of $[(\mathbf{L})_3Fe]^{2+}$) yields a straight line with an intercept equal to ln(A) and a slope of $-E_a/k_B$ (Figure S15a). The magnitude of E_a was found to be 1300 ± 50 cm^{-1}, which is significantly higher than has been reported for any Fe(II) chromophores of which we are aware. For example, the corresponding value for $[Fe(bpy)_3]^{2+}$ is 310 ± 15 cm^{-1},[66] meaning the activation energy associated with the ground-state recovery (GSR) of $[(\mathbf{L})_3Fe]^{2+}$ is four-fold larger than in $[Fe(bpy)_3]^{2+}$, twice that observed in Fe(II) complexes supported by robust hexadentate N_6 donor sets,[69] and even exceeds values reported for various Co(III) bipyridine complexes (E_a = 850 – 1200 cm^{-1})[63] which efficiently populate ^{3}MC excited states in the Marcus inverted region. For further context, the tetracarbene-dipyridyl photosensitizer, *bis*(1,1'-(pyridine-2,6-diyl)*bis*(3-methylimidazol-2-ylidene))iron(II) dication $\{[Fe(C\hat{}N\hat{}C)_2]^{2+}\}$, has a reported activation barrier of 790 cm^{-1} (but a ^{3}MC excited-state lifetime of only ~10 ps at room temperature).[68]

Transition state theory, derived from statistical mechanics, recasts the problem through the Eyring equation in terms of the free energy of the system (in contrast to the Arrhenius model which

is largely empirical in nature). A plot of $\ln(k_{obs}/T)$ vs 1/T (Figure S15b) yields the activation enthalpy ($\Delta H^{\ddagger}$) from the slope while the activation entropy ($\Delta S^{\ddagger}$) can be extracted from the intercept (provided there is information and/or assumptions about the transmission coefficient (κ) for the reaction). In the adiabatic limit (*i.e.*, $\kappa = 1$), one obtains values of $\Delta S^{\ddagger} = -3.20 \pm 0.50$ cm^{-1} K^{-1} and $\Delta H^{\ddagger} = 1125 \pm 50$ cm^{-1} for $[(\mathbf{L})_3Fe]^{2+}$ in THF solution. At roughly half of the value typically found for Fe(II) complexes that involve relaxation from a $^5T_2$ high-spin state (-4.68 to -8.53 cm^{-1} / K)[70,71] and similar to that found for Co(III) polypyridyl complexes, the magnitude of $\Delta S^{\ddagger}$ implicates a $^3T_1$ state as the lowest-energy excited state of $[(\mathbf{L})_3Fe]^{2+}$.

Finally, a semi-classical Marcus treatment was applied. In this approach, the Marcus relation combining driving force (ΔG^0) and reorganization energy (λ) replaces the free energy of activation. Using DFT to estimate the driving force ($\Delta G^0 = -5220$ cm^{-1}; *vide infra* as well as the Supporting Information), we determine a reorganizational energy of $\lambda = 14\ 200 \pm 500$ cm^{-1} and electronic coupling between the two states (H_{ab}) equal to 34.0 ± 5.0 cm^{-1} (Figure 5, Table 1). It should be noted that the quadratic relationship between the non-radiative rate constant (*i.e.*, ground-state recovery) and the driving force/reorganization energy predicted by Marcus theory yields two possible values for λ, specifically 14 200 cm^{-1} and 1 900 cm^{-1}. In our view, only the larger value is reasonable for the distortions that typically accompany formation of a MC excited state.[63,66]

To avoid placing undue weight in drawing our conclusions on the accuracy of a DFT-calculated driving force (which may be clouded by the nature of the coordination environment in $[(\mathbf{L})_3Fe]^{2+}$ that includes strong intramolecular forces imposed by π-stacking), we evaluated values for the electronic coupling in four additional ways: (1) by employing driving forces calculated from single-point calculations using the same functional (O3LYP) but varying the amounts of

Hartree-Fock (HF) exchange included; (2) employing different functionals, which themselves include different amounts of HF exchange (TPSSh, O3LYP, B3LYP and PBE0);[72] (3) by calculating the range of λ obtained using a range of driving forces representing what we consider to be the highest and lowest physically plausible magnitudes; and (4) by considering a range of values of λ we considered physically meaningful. In all cases, the value of H_{ab} is only minimally affected (see Figures S16 and S17). In the semi-classical Marcus theory treatment, the intercept of the experimental plot of $\ln(k_{nr} T^{1/2})$ vs 1 / T is proportional to H_{ab}^4 / λ (Figure 5); here, H_{ab}^4 / λ = 97 cm^{-3}. The fourth-power dependence significantly attenuates the influence of λ on the value of H_{ab}, thus giving rise to the (relatively) narrow range of values for H_{ab} that are possible and still be consistent with the experimental results.

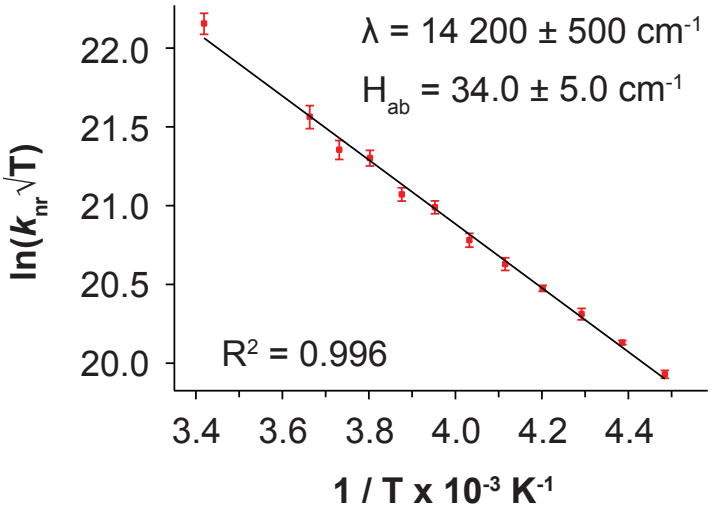

Figure 5. *Plot of variable-temperature ground-state recovery kinetics acquired for* $[(\mathbf{L})_3Fe]^{2+}$ *in THF solution between 223 and 293 K. The solid line corresponds to a fit of the data to the semi-classical formulation of Marcus theory. See text for additional details.*

The electronic coupling (H_{ab}) describes the degree of electronic communication between the two states involved in the GSR; that is, the lowest-energy excited state and the ground state.

H_{ab} is typically much smaller for coupling between quintet and singlet states—as would be present should the long-lived excited state of $[(\mathbf{L})_3Fe]^{2+}$ have $^5T_2$ character—as these states interact through the ^{3}MC state via second-order coupling.[66] For example, electronic coupling between the $^1A_1$ ground-state and the $^5T_2$ excited state of $[Fe(bpy)_3]^{2+}$ (4.4 ± 0.2 cm^{-1}) or $[Fe(tpy)_3]^{2+}$ (6.2 ± 1.2 cm^{-1}) is 5-7 times smaller than the value we extracted from the variable-temperature data on $[(\mathbf{L})_3Fe]^{2+}$ (Table 1), an observation that reinforces our assignment of the lowest energy excited state of $[(\mathbf{L})_3Fe]^{2+}$ as the $^3T_1$ ligand-field state. Direct electronic communication between the $^1A_1$ ground state and a $^3T_1$ excited state is expected to be inversely proportional to the energy difference between them. This is a consequence of simple perturbation theory: as the energy difference between two states that are directly coupled varies, the magnitude of the interaction changes accordingly. Such an inverse relationship between the energy gap and H_{ab} was experimentally verified in the aforementioned series of Co(III) polypyridyls.[63] The H_{ab} value obtained for $[(\mathbf{L})_3Fe]^{2+}$ is slightly higher than what was determined for the Co(III) polypyridyls, thereby suggesting that the $^3T_1$ state sits at lower energy (i.e., a smaller excited-state/ground-state gap) in $[(\mathbf{L})_3Fe]^{2+}$ as compared to the Co(III) complexes.

Table 1. Analysis of vtTA data for $[(\mathbf{L})_3Fe]^{2+}$ and literature comparisons (--- indicates data is unavailable).

Compound	E_a / cm^{-1}	$\Delta H^{\ddagger}$ / cm^{-1}	$\Delta S^{\ddagger}$ / cm^{-1}/K	λ / cm^{-1} [e]	H_{ab} / cm^{-1} [e]	τ (293 K) [f] / ns	τ (T) [f] / ns	Excited-State Assignment [g]
$[Fe(bpy)_3]^{2+}$ [a]	310 ± 15	125 ± 20	- 5.66 ± 0.07	11 000 ± 1000	4.4 ± 0.2	1.05	1.52 (235 K)	$^5T_2$
$[Fe(tpy)_2]^{2+}$ [a]	755 ± 70	465 ± 10	-5.58 ± 0.02	14 100 ± 1200	6.2 ± 1.2	5.2	12.6 (235 K)	$^5T_2$
$[Co(pyro\text{-}bpy)_3]^{3+}$ [b]	850 ± 50	655 ± 40	-3.30 ± 0.15	5 700 ± 500	25.5 ± 1.0	0.47 ± 0.02	0.80 (258 K)	$^3T_1$
$[Co(4,4'\text{-}deeb)_3]^{3+}$ [b]	1200 ± 50	1010 ± 40	-3.93 ± 0.15	5 500 ± 500	16.5 ± 1.5	6.60 ± 0.80	14.6 (258 K)	$^3T_1$
$[Fe(C\text{^}N\text{^}C)_2]^{2+}$ [c]	790	---	---	---	---	~0.010	0.190 (130 K)	$^3T_1$
$[(\mathbf{L})_3Fe]^{2+}$ [d]	1300 ± 50	1125 ± 50	-3.20 ± 0.50	14 200 ± 500	34.0 ± 5.0	4.1 ± 0.3	33.0 ± 0.8 (223 K)	$^3T_1$

[a] From reference [66], data collected in CH_3CN. The Eyring analyses were taken from ref [73]

[b] From reference [63], data collected in CH_3CN

[c] From reference [68], data collected in butyronitrile

[d] Data collected in THF

[e] Determined using DFT single-point calculated driving force, ΔG^0 = -5220 cm^{-1} (RIJCOSX-DEF2/J-SMD-O3LYP-D4/def2-TZVP//RIJCOSX-SMD-O3LYP-D4/def2-SVP)

[f] Rate of ground-state recovery from longest-lived excited state, experimental data collected here done in THF

[g] $^3T_1$ assignment is based on octahedral symmetry and is not strictly correct due to the lower symmetry of these pseudo-octahedral molecules. Based on the orbital picture for $[(\mathbf{L})_3Fe]^{2+}$ (Figure S18) one might postulate a doubly degenerate state, ^3E, but what is known is that it is a low energy triplet state that would be of lower symmetry than $^3T_1$, and splitting of this higher symmetric excited state may be one factor contributing to the stability of the ^{3}MC state populated for $[(\mathbf{L})_3Fe]^{2+}$ (*vide infra*)

Computational Analysis and Discussion. At the ground-state geometry, the Tanabe-Sugano diagram for octahedral d^6 Fe(II) shows that the ligand field can be increased to the point where the $^5T_2$ and $^3T_1$ excited states cross and the triplet state becomes the lower energy of the two.[74] Outside the Frank-Condon region, this energetic ordering can change as nuclei respond to the new force fields experienced in electronic excited states. Optimization of the three relevant electronic states of $[(\mathbf{L})_3Fe]^{2+}$ ($S = 0, 1, 2$) using spin-unrestricted DFT calculations is consistent with ^{3}MC character for the lowest energy excited state: the optimized energy of the $S = 2$ state is nearly twice as high as the optimized $S = 1$ state, in keeping with the established photophysics of Fe(II) carbene complexes.[35] The optimized excited-state structures are also consistent with the experimentally determined entropy of activation ($\Delta S^{\ddagger}$), representing the change in entropy from the excited state to the transition state on route to ground-state (GS) recovery. The bond lengths calculated for the ^{5}MC state are significantly longer than in the ^{3}MC state (Table S7) and therefore a larger molecular volume change should accompany direct $^5MC \rightarrow {}^1GS$ relaxation compared to $^3MC \rightarrow {}^1GS$. While these results provide further support for the assignment of the lowest energy excited state as a ^{3}MC state, they do not, however, explain why this typically rapidly decaying state might be so long-lived for $[(\mathbf{L})_3Fe]^{2+}$.

Using the difference in the zero-point corrected energies of the optimized $S = 1$ and $S = 0$ states, we could calculate the driving force (ΔG^0 = -5220 cm^{-1}) and consequently the reorganizational energy (λ = 5150 cm^{-1}) for the $^3MC \rightarrow {}^1GS$ ground-state recovery.[63] That a higher value of λ (14 200 ± 500 cm^{-1}) was determined from experiment can be explained in part due to the fact that the experimental value corresponds to the total reorganization energy for the excited-state to ground-state conversion, whereas our modelling accounts only for inner-sphere contributions. Even with this caveat, it seems unlikely that outer-sphere contributions – which

largely result from solvent reorganization[75] – are of sufficient magnitude to make up the difference between the experimental and theoretical values obtained for λ. Instead, we believe that the discrepancy reflects the difficulty in accurately modelling $[(\mathbf{L})_3Fe]^{2+}$, in particular with regard to the energetics of the inter-ligand π-stacking interactions described above.

In the ground state, the longest Fe-N interaction (XRD: 2.230 Å, DFT GS: 2.204 Å) is *trans* to the carbene. In the optimized triplet state, this distance contracts significantly (ΔDFT = -0.088 Å) while the two mutually *trans* Fe-N phenanthridinyl distances elongate (ΔDFT = +0.260 and +0.365 Å, respectively; Figure 6a). These distortions are quite significant for a ^{3}MC excited state. In comparison, the population of e_g* Fe-L σ-anti-bonding orbitals which accompanies formation of the $^3T_1$ excited state in $[Fe(bpy)_3]^{2+}$ results in Fe-N elongations of only ~0.1 Å.[76] Even in the $^3T_1$ state of the heteroleptic $[Fe(btz)_2(bpy)]^{2+}$ {btz = bis(1,2,3-triazol-5-ylidene)}, the Fe-bpy distance elongates only by ~0.2 Å, attributed to the higher electron density about the Fe center thanks to the inclusion of four mesoionic carbene donors.[39] From an orbital perspective, the reorganization of electron density in the ^{3}MC excited state of $[(\mathbf{L})_3Fe]^{2+}$ destabilizes the $d_{x^2-y^2}$ orbital while in turn stabilizing the d_z^2 orbital, which becomes the highest singly occupied molecular orbital (Figure 6b). In contrast, the Fe-$C_{carbene}$ distances in the ^{3}MC excited state elongate by 0.008, 0.044 and 0.095 Å, less than the ~0.1 Å change in the corresponding Fe-$C_{carbene}$ distances in $[Fe(btz)_2(bpy)]^{2+}$.[39] The retention of strong equatorial metal-ligand interactions could contribute to the anomalous stability of the ^{3}MC state, which lies 0.61 eV above the ground state compared to 0.67 eV for the ^{3}MC minimum of $[Fe(btz)_2(bpy)]^{2+}$ [39] and 1.24 eV for the corresponding excited state of $[Fe(bpy)_3]^{2+}$ (Table S8).[77] Essentially, the Fe-$C_{carbene}$ and equatorial Fe-N bonds stay tightly bound to the metal center, pushing electron density into the equatorial $d_{x^2-y^2}$ plane while elongation along the axial Fe-N bonds leads to less electron density along the d_{z^2} plane. This elongation-type

Jahn-Teller distortion allows for stabilization of the $^3T_1$ state, as the d_{z^2} orbital is energetically closer to the nominally t_{2g} orbitals, resulting in a stable ^{3}MC excited state.

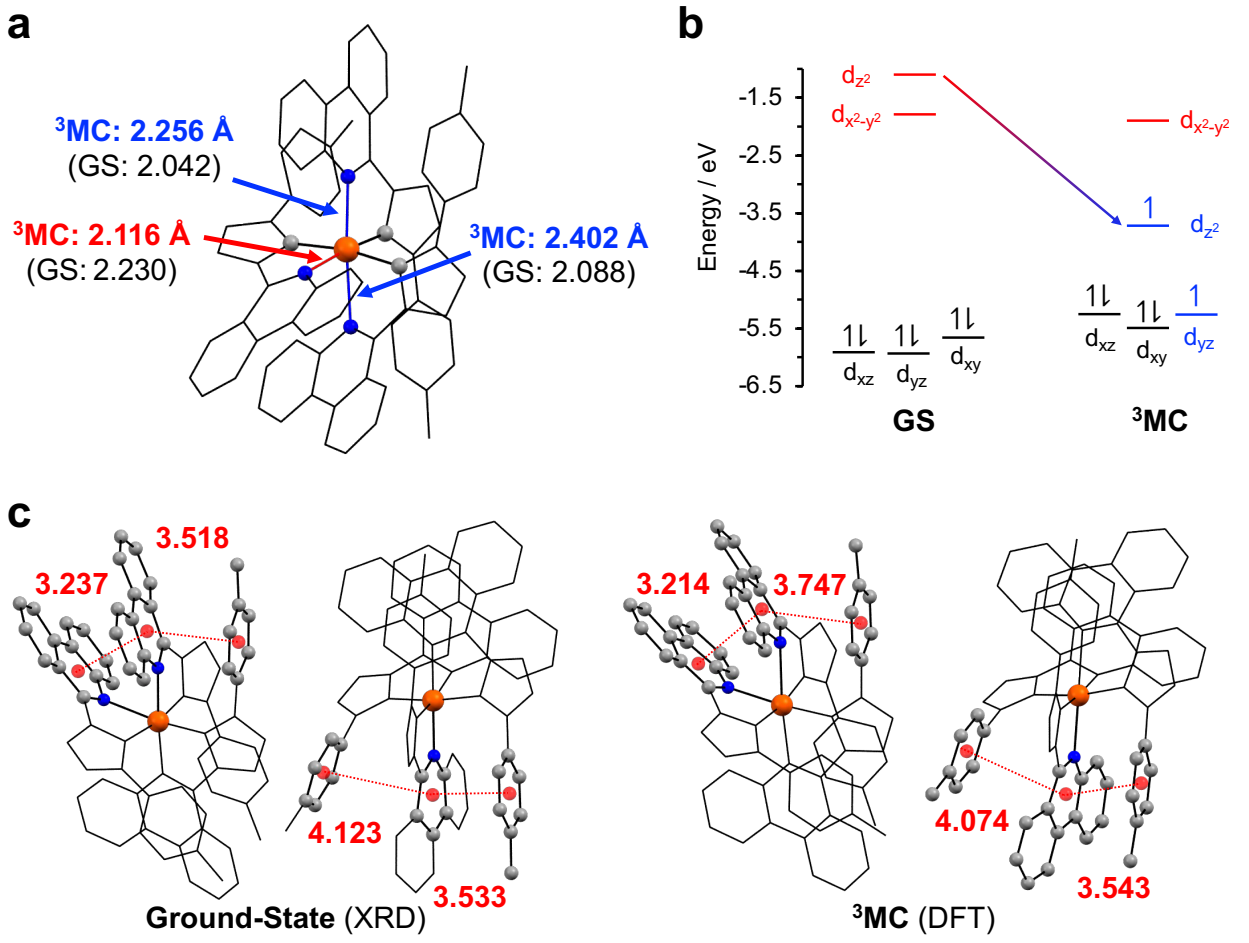

Figure 6. *Jahn-Teller distortion in the $^3T_1$ state highlighted through (a) changes in bond distances and (b) impact on orbital energies, with prominent π-stacking distances in the ground-state (S_0) and excited $^3T_1$ state shown in (c).*

A further contributing factor is inter-ligand π-stacking, a tactic previously used to improve the photophysical properties of emissive Ir(III) and Re(I) complexes through enhanced rigidity.[78–80] The π-stacking observed in the solid-state structure (i.e., the electronic ground state) of $[(\mathbf{L})_3Fe]^{2+}$

is retained in the optimized ^{3}MC state (Figure 6c). The distances between ligand ring centroids remain within typical π-stacking distances and in fact shorten in some instances (XRD: 3.237-4.123 Å; ^{3}MC: 3.214-4.074 Å).[81,82] We believe these intramolecular interactions further retard the metal-ligand bond flexibility and torsional rotation modes required for relaxation to the ground state,[38] ultimately contributing to the large activation energy (E_a), high enthalpic barrier ($\Delta H^{\ddagger}$), and corresponding elongation of the excited state lifetime. Along with hindering relaxation of the triplet excited state to the ground state, this intramolecular π-stacking likely diminishes the efficiency of populating the ^{5}MC state as the quintet state lies further along the PES with even more pronounced molecular reorganization (Figure S19). Torsional modes have been shown to be vital to $^5T_2 \rightarrow {}^1A_1$ ground-state recovery in iron(II) polypyridyl complexes.[69,83] The deviation from octahedral symmetry does not significantly differ between the ground-state (14°) and the ^{3}MC state (16°), but is a substantial 30° in the optimized structure of the quintet state. Interestingly, this phenomenon might also contribute to the long ^{3}MLCT lifetime (528 ps) of $[Fe(btz)_3](PF_6)_2$, as the crystal structure displays π-stacked rings (ring centroid distance = 3.821-4.003 Å, average = 3.929 Å).[41]

We can now assemble a more complete picture of the potential energy landscape (Figure 7). Optical excitation forms a $^{1/3}$MLCT excited state which rapidly decays down to a ^{3}MC excited state on the order of a picosecond, followed by relaxation back to the ground state with a time constant of 4.1 ± 0.3 ns at 293 K. The barrier between the ^{3}MC excited and ^{1}GS state is reasonably large and was quantified in terms of an Arrhenius activation energy of E_a = 1300 ± 50 cm^{-1} based on data from variable-temperature time-resolved absorption measurements. The magnitude of this barrier reflects a significant difference in energy between the ^{3}MC minimum and the minimum-energy crossing point (MECP) with ^{1}GS. The sizeable $\Delta H^{\ddagger}$ and small volume change denoted by

the smaller value of $\Delta S^{\ddagger}$ suggests the MECP is likely not far from the ^{3}MC minimum along the metal-ligand bond coordinate. This, together, suggests a narrowing of the potential wells representing various electronic states resulting from the increased rigidity wrought by inter-ligand, intramolecular π-stacking. The large reorganizational energy derives from significant reorganization in the relaxed ^{3}MC state compared to the ground state geometry manifesting in a significant Jahn-Teller distortion and relatively stable triplet excited state, as supported by computational modelling. This distortion implies the ^{3}MC state is not nested in the ^{1}GS potential surface but rather is positioned outside—a hallmark of the 'Marcus normal regime'. While this is not reproduced by DFT (the ^{1}GS state is calculated to be lower in energy at the optimized ^{3}MC geometry – see Figure S19, Table S8), the states are very close in energy and within the error of DFT. In addition to being energetically destabilized, the ^{5}MC state is even more significantly distorted from the ground-state geometry, evidenced by the calculated octahedricity parameters[84] of each state along with the calculated bond lengths/angles (Figures S19 and S22; Table S7).

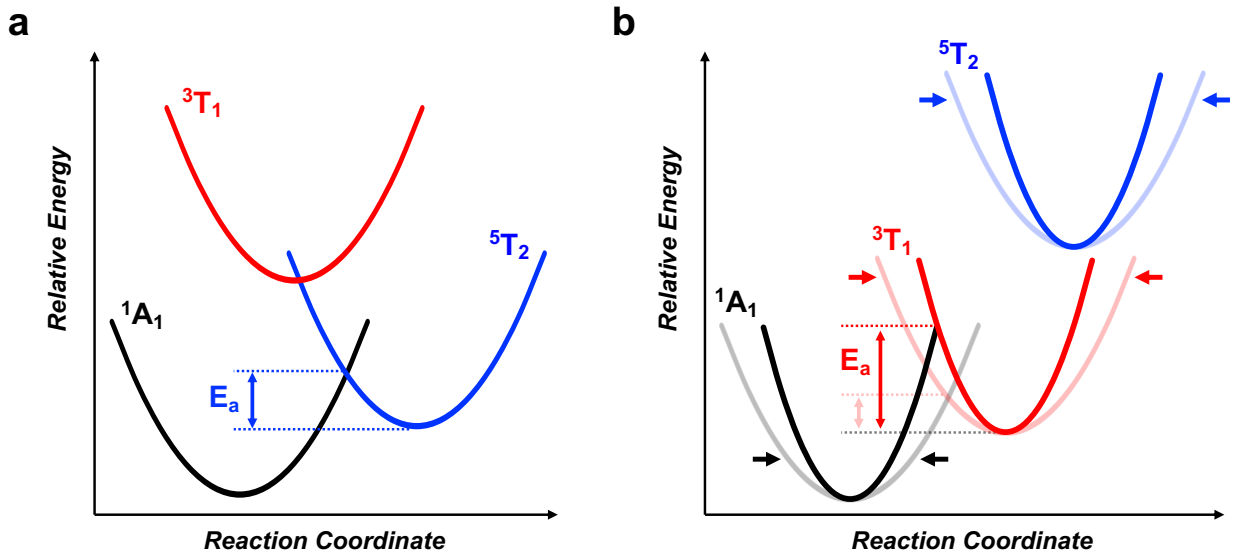

Figure 7. *Schematic simple potential energy diagrams depicting (a) the typical ligand-field excited state ordering for Fe(II) polypyridyls such as* $[Fe(bpy)_3]^{2+}$*; and (b) the effect on the activation energy (*E_a*) on introducing strong-field carbene ligands with the added impact of increased rigidity through inter-ligand, intramolecular, π-stacking shown in the narrowing of the potential wells (horizontal arrows).*

CONCLUSIONS

The search for molecular design tactics to control relaxation cascades and lengthen the lifetimes of particular excited states has yielded spectacular results in terms of charge-transfer excited states, but long-lived triplet metal centered states of Fe(II) have so far remained elusive. Here, we show how a unique ligand architecture leveraging strong-field donors and rigidity through intramolecular π-stacking can be exploited to access just such a unique temporal decay cascade. The initially formed charge transfer-state manifold relaxes to the lower energy ligand-field manifold in *ca.* 1 picosecond, ultimately forming a $S = 1$ ligand-field state as the lowest energy excited state of the system. This excited state exhibits a time constant of 4.1 ± 0.3 ns at ambient temperature, extending to 33.0 ± 0.8 ns at 223 K, which is unprecedented for an Fe(II)-based chromophore. This exceptionally long triplet lifetime is attributed to inter-ligand π-stacking facilitated by the combination of carbene-tolyl substituents and benzannulated phenanthridinyl donors conspiring with a Jahn-Teller stabilized excited state to generate a high activation barrier for ground-state recovery and what we believe to be the longest ^{3}MC excited state on record.[85,86] On-going work includes time-resolved X-ray studies, which will provide detailed information concerning both the structure (X-ray scattering) and spin (X-ray emission) associated with the lowest-energy excited state, as well as studies geared toward probing how to balance increasing the stored potential associated with the ^{3}MC excited state in the form of zero-point energy while maintaining a sufficiently long lifetime to enable its use in bimolecular reaction chemistry.

EXPERIMENTAL DETAILS

Unless otherwise stated, all air sensitive manipulations were carried out inside an inert-atmosphere glove box (N_2) or using standard Schlenk techniques (Ar). Chemicals *p*-toluidine (Alfa Aesar) and $FeBr_2$ (Aldrich) were purchased from commercial suppliers as reagent grade or better and used as received. 6-chlorophenanthridine[87] was synthesized following a published procedure. Organic solvents were dried over appropriate reagents and deoxygenated prior to use when inert conditions were needed. NMR spectra were recorded on a Bruker Avance 300 MHz (UM), a Bruker Avance-III 500 MHz (UM) or an Agilent DDR2 500 MHz (MSU) spectrometer. ^{1}H and $^{13}C\{H\}$ NMR spectra were referenced to residual solvent peaks. High-resolution mass spectra were collected using a Bruker microOTOF-QIII. Elemental analysis was performed by the Analytical & Instrumentation Laboratory at the University of Alberta, College of Natural and Applied Sciences.

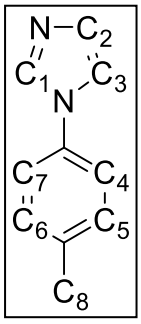

Synthesis of *N*-tolylimidazole: The procedure was adapted from the reported synthesis of a similar imidazole.[88] Glacial acetic acid (10 mL), aqueous formaldehyde (3.0 mL, 40 mmol) and aqueous glyoxal (4.6 mL, 40 mmol) was heated in an oil bath set to 70°C with stirring. Another solution was made containing *p*-toluidine (4.29 g, 40.0 mmol), ammonium acetate (3.08 g, 40.0 mmol) in water (2 mL) and glacial acetic acid (10 mL); and was added dropwise over 30 min. The resulting solution was continued to stir in an oil bath set to 70°C for 18 h. The reaction mixture was cooled to room temperature and added dropwise to a saturated aqueous solution of sodium bicarbonate (30 g in 300 mL), which was then stirred at room temperature for 30 min. The product was extracted with hexanes (4 x 150 mL). The combined organic layers were dried with magnesium sulfate, filtered and the solvent was removed under reduced pressure giving a spectroscopically pure light-yellow solid. Yield = 3.04 g (48%).

Spectroscopic data matched that found in literature.[89] ^{1}H NMR ($CDCl_3$, 300 MHz, 22°C): δ 7.81 (t, J_{HH} = 1.2 Hz, 1H; C_1H), 7.26 (s, 4H; $C_{4\text{-}7}H$), 7.24 (t, J_{HH} = 1.4 Hz, 1H; C_3H), 7.19 (t, J_{HH} = 1.2 Hz, 1H; C_2H), 2.40 ppm (s, 3H; C_8H). $^{13}C\{^{1}H\}$ NMR ($CDCl_3$, 75 MHz, 22 °C): δ 137.6 (C_{quat}), 135.8 (C_1), 135.2 (C_{quat}), 130.5 ($C_{4,7}$), 130.4 (C_2), 121.6 ($C_{5,6}$), 118.5 (C_3), 21.1 ppm (C_8).

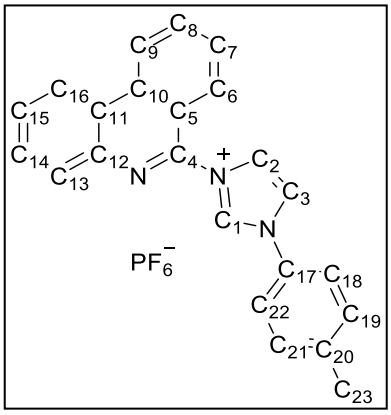

Synthesis of (*N*-tolyl-*N*'-phenanthridinyl)imidazolium hexafluorophosphate ([LH]PF_6): A 50 mL Teflon-stoppered flask was charged with 6-chlorophenanthridine (0.178 g, 0.83 mmol) and *N*-tolylimidazolium (0.171 g, 1.08 mmol). The solids were dried under vacuum for 30 min and the flask was backfilled with Ar. The mixture was heated neat while stirring for 3 h in an oil bath set to 170 °C, the starting materials melted and the product solidified out. The resulting solid was cooled to room temperature and extracted from the flask with a minimal amount of CH_2Cl_2 (8 mL). The solution was then added dropwise to 100 mL diethyl ether resulting in an off-white solid which was collected via vacuum filtration. The solid was then re-dissolved in minimal methanol (~10 mL) and a saturated solution of aqueous KPF_6 (1.53 g, 8.31 mmol) was added. A white solid precipitated out immediately and the mixture was stirred at room temperature for 16 h. The solid was collected and washed with water (50 mL) and followed with diethyl ether (50 mL). A spectroscopically pure white solid was collected. Yield = 0.312 g (78%). ^{1}H NMR (DMSO-d_6, 300 MHz, 22°C): δ 10.55 (t, J_{HH} = 1.6 Hz, 1H; C_1H), 9.13 (d, J_{HH} = 8.4 Hz, 1H; C_9H), 9.03 (dt, J_{HH} = 7.9, 2.9 Hz, 1H; $C_{15}H$), 8.67 (d, J_{HH} = 1.6 Hz, 2H; $C_{2,3}H$), 8.28 (d, J_{HH} = 8.2 Hz, 1H; $C_{13}H$), 8.21 (m, 2H; $C_{7,8}H$), 7.97 (m, 3H; $C_{6,14,16}H$), 7.87 (d, J_{HH} = 8.5 Hz, 2H; $C_{18,22}H$), 7.54 (d, J_{HH} = 8.2 Hz, 2H; $C_{19,21}H$), 2.45 ppm (s, 3H; $C_{23}H$). $^{13}C\{^{1}H\}$ NMR (DMSO-d_6, 75 MHz, 22 °C): δ 145.6

(C_{12}), 141.3 (C_4), 140.1 (C_{17}), 136.5 (C_1), 134.7 (C_{10}), 133.1(C_8), 132.4 (C_{20}), 130.4 ($C_{19,21}$), 130.3 (C_{16}), 129.6 (C_7), 129.4 (C_6), 129.2 (C_{14}), 125.8 (C_{13}), 124.7 (C_5), 124.2 (C_2), 123.3 ($C_{9,15}$), 122.3 ($C_{18,22}$), 121.9 (C_3), 120.2 (C_{11}), 20.6 ppm (C_{23}). ^{19}F-NMR (DMSO-d_6, 282 MHz, 22 °C): δ -68.9 (s, PF_6), -71.4 ppm (s, PF_6). HR-MS (APCI-TOF) m/z: $[M]^+$ calculated for $[C_{23}H_{18}N_3]^+$: 336.1495; found: 336.1503.

Synthesis of $[(L)_3Fe](PF_6)_2$: [**L**H]PF_6 (0.100 g, 0.21 mmol) was weighed into a 50 mL bomb flask, followed by $FeBr_2$ (0.015 g, 0.069 mmol) and THF (5 mL). The mixture was refluxed and stirred in an oil bath set to 100°C for 16 h. The reaction was then cooled down to room temperature and a solution of potassium *tert*-butoxide (0.026 g, 0.229 mmol) in THF (4 mL) was added, causing an immediate color change to dark purple. Stirring was continued at room temperature for 2 h, after which the solvent was evaporated under reduced pressure. The solid was dissolved in acetonitrile (3 mL) and filtered into an aqueous solution of KPF_6 (0.064 g, 0.346 mmol; in 15 mL H_2O). The suspension was stirred at room temperature for 16 h and then filtered through Celite. The precipitate was washed with H_2O (30 mL), diethyl ether (30 mL) and then pulled through the Celite pad with acetonitrile (20 mL). The acetonitrile fraction was dried under reduced pressure and cleaned via column chromatography on silica with a MeOH/DCM gradient (0-10%). The combined red fractions were then recrystallization using acetonitrile/diethyl ether layering, resulting in a dark red solid. Yield = 0.031 g (33%). ^{1}H NMR (CD_3CN, 500 MHz, 22°C): δ 8.77 (d, J_{HH} = 8.4 Hz, 1H; $^{phen}C_{Ar}H$), 8.61 (d, J_{HH} = 8.1 Hz, 1H; $^{phen}C_{Ar}H$), 8.36 (d, J_{HH} = 2.5 Hz, 1H; $^{imidazole}C_{Ar}H$), 8.29 (d, J_{HH} = 2.2 Hz, 1H; $^{imidazole}C_{Ar}H$), 8.20 (d, J_{HH} = 8.7 Hz, 1H; $^{phen}C_{Ar}H$), 8.18 (d, J_{HH} = 2.1 Hz, 1H; $^{imidazole}C_{Ar}H$), 8.12 (m, 1H; $^{phen}C_{Ar}H$), 8.01 (ddd, J_{HH} = 8.4, 5.1, 3.2 Hz, 1H; $^{phen}C_{Ar}H$), 7.94 (m, 3H; $^{phen}C_{Ar}H$), 7.84 (m, 1H; $^{phen}C_{Ar}H$), 7.81 (m, 2H; $^{phen}C_{Ar}H$), 7.71 (t, J_{HH} =

7.7 Hz, 1H; $^{phen}C_{Ar}H$), 7.69 (d, J_{HH} = 2.1 Hz, 1H; $^{imidazole}C_{Ar}H$), 7.65 (m, 3H; $^{phen}C_{Ar}H$), 7.57 (t, J_{HH} = 7.5 Hz, 1H; $^{phen}C_{Ar}H$), 7.48 (m, 3H; $^{phen}C_{Ar}H$, $^{imidazole}C_{Ar}H$), 7.42 (m, 2H; $^{phen}C_{Ar}H$), 7.37 (d, J_{HH} = 2.5 Hz, 1H; $^{imidazole}C_{Ar}H$), 7.34 (t, J_{HH} = 7.6 Hz, 1H; $^{phen}C_{Ar}H$), 7.25 (d, J_{HH} = 8.3 Hz, 1H; $^{phen}C_{Ar}H$), 7.15 (d, J_{HH} = 8.3, 1H; $^{phen}C_{Ar}H$), 7.04 (ddd, J_{HH} = 8.5, 6.7, 1.2 Hz, 1H; $^{phen}C_{Ar}H$), 6.95 (br d, J_{HH} = 7.8 Hz, 1H; $^{tolyl}C_{Ar}H$), 6.66 (br m, 6H; $^{tolyl}C_{Ar}H$), 6.29 (br s, 2H; $^{tolyl}C_{Ar}H$), 5.94 (br d, J_{HH} = 7.9 Hz, 1H; $^{tolyl}C_{Ar}H$), 5.84 (br d, J_{HH} = 7.7 Hz, 1H; $^{tolyl}C_{Ar}H$), 5.81 (br d, J_{HH} = 8.1 Hz, 1H; $^{tolyl}C_{Ar}H$) 2.29 (s, 3H; $^{tolyl}CH_3$), 1.56 (s, 3H; $^{tolyl}CH_3$), 1.31 ppm (s, 3H; $^{tolyl}CH_3$). $^{13}C\{^1H\}$ NMR (CD_3CN, 126 MHz, 22 °C): δ 209.8 (C_{NHC}), 207.1 (C_{NHC}), 203.7 (C_{NHC}), 156.1 (NC_{phen}), 155.5 (NC_{phen}), 154.4 (NC_{phen}), 143.8 (C_{phen}), 141.6 (C_{phen}), 141.4 (C_{phen}), 141.2 (C_{phen}), 140.5 (C_{tol}), 140.2 (C_{tol}), 136.6 (C_{tol}), 135.8 (C_{tol}), 135.7 (C_{tol}), 135.2 (C_{phen}), 134.5 (C_{phen}), 134.0 (C_{phen}), 133.9 (C_{phen}), 133.6 (C_{phen}), 133.6 (C_{phen}), 131.0 (C_{tol}), 130.9 (C_{tol}), 130.1 (C_{phen}), 130.1 (C_{phen}), 130.1 (C_{imid}), 129.7 (C_{tol}), 129.7(C_{phen}), 129.6 (C_{imid}), 129.2 (C_{imid}), 128.9 (C_{phen}), 128.8 (C_{phen}), 128.7 (C_{phen}), 128.6 (C_{phen}), 128.6 (C_{phen}), 128.5 (C_{tol}), 128.5 (C_{tol}), 128.3 (C_{phen}), 127.9 (C_{tol}), 127.8 (C_{phen}), 127.0 (C_{imid}), 127.0 (C_{tol}), 126.1 (C_{phen}), 125.9 (C_{tol}), 125.5 (C_{imid}), 124.9 (C_{tol}), 124.6 (C_{phen}), 124.4 (C_{phen}), 124.0 (C_{phen}), 124.0 (C_{imid}), 123.8 (C_{phen}), 123.7 (C_{phen}), 123.7 (C_{phen}), 123.5 (C_{phen}), 123.4 (C_{phen}), 123.4 (C_{phen}), 123.3 (C_{phen}), 123.3 (C_{imid}), 123.0 (C_{phen}), 119.1 (C_{phen}), 117.9 (C_{phen}), 117.1 (C_{phen}), 21.1 (C_{Me}), 20.6 (C_{Me}), 20.1 ppm (C_{Me}). Four tolyl ^{13}C resonances were not found, likely due to the broad nature of some of these peaks observed in both the ^{13}C and ^1H spectra. ^{19}F NMR (CD_3CN, 471 MHz, 22 °C): δ -72.1 (s, PF_6), -73.6 ppm (s, PF_6). HR-MS (APCI-TOF) m/z: $[M]^{2+}$ calculated for $[C_{69}H_{51}FeN_9]^{2+}$: 530.6804; found: 530.6789. UV-Vis (THF, 22 °C): 325 (shoulder), 342 (15 800), 505 nm (8 040 M^{-1} cm^{-1}). Anal. Calc. for $C_{69}H_{51}F_{12}Fe_1N_9P_2$: C, 61.30; H, 3.80; N, 9.32 %. Found: C, 61.49; H, 3.96; N, 9.33 %.

UV-Vis Absorbance: Electronic absorption spectra were acquired on solutions prepared under ambient conditions in CH_3CN or THF in 1 cm path length quartz cuvettes using a PerkinElmer Lambda 1050 spectrophotometer; spectra measured before and after all transient absorption measurements (collected to ensure integrity of the samples) were collected on a Varian Cary50 spectrophotometer.

Electrochemistry: For electrochemical analysis, a 1 mM solution of complex, and 0.1 M of $[n\text{Bu}_4\text{N}]\text{PF}_6$ as electrolyte, was made in 15 mL of acetonitrile and performed under argon. Electrochemical experiments were preformed using a CHI 760c bipotentiostat, a 3 mm diameter glassy carbon working electrode, a Ag/Ag^+ non-aqueous quasi-reference electrode separated by a Vycor tip, and a Pt wire counter electrode. Cyclic voltammetry was conducted using scan rates of 100-500 mV/s. Differential Pulse Voltammetry was performed using a 5 mV increment, 50 mV amplitude, 0.05 s pulse width, 0.0167 s sample width, and 0.5 s pulse period. Following the experiment ferrocene was added to the solution as an internal standard and all potentials are reported versus the $FcH^{0/+}$ redox couple.

Spectroelectrochemistry: Spectroelectrochemical data were collected on an Agilent Cary 5000 Series UV-Vis NIR spectrophotometer using a CHI-620C electrochemical analyzer and a room temperature optically transparent thin-layer electrochemical (OTTLE) cell. A 3-electrode system of Pt minigrid (32 wires/cm) working and auxiliary electrodes and an Ag wire pseudo-reference electrode was used.[90]

Time-resolved Absorption Spectroscopy: Femtosecond time-resolved absorption data were acquired using a spectrometer that has been described previously.[91] Briefly, a Ti:sapphire oscillator (Coherent Mira) pumped by a solid state diode laser operating at 5.0 W provided a 400 mW (76 MHz) mode-locked pulse train that seeded a Ti:sapphire regenerative amplifier (Positive Light). The output (800 nm, 1KHz, IRF ~ 130 fs) is split 70/30 into pump and probe beams, respectively. The pump portion is sent to an optical parametric amplifier (Light Conversion TOPAS), generating tunable visible light, while the probe portion is focused into a sapphire crystal to generate a white light continuum. The pump output is directed to a four-pass delay line that provides a delay range of ~13.2 ns for data collection. Probe wavelengths were selected by passing the continuum through 10 nm bandpass filters (Thor Labs) of the desired wavelength range, then focused on to an amplified Si photodiode. All data were acquired with the pump and probe beam set at a relative angle of 54.7° to eliminate anisotropic effects; the amplitudes of the signals were all checked to ensure linear response. Samples were prepared in either spectral grade CH_3CN or THF that had been dried via distillation prior to use and placed in a 1 mm quartz cuvette. Sample absorbances were adjusted to maximize signal-to-noise in different regions of the spectrum but were typically in the range of 0.5 ± 0.3. All ultrafast data were collected at room temperature (293 K). Data fitting was performed using Igor Pro software. All experiments were done at least 3 separate times, with the data averaged between the runs. The error in the lifetime was determined from the fit, added to and subtracted from the lifetime of that run to get the lower and higher limits, and then the standard deviation between the experiments was taken to provide the error bars cited. Following all experiments, a UV-Vis was taken of the sample and compared to an absorbance spectrum taken before to confirm the sample integrity. Full spectrum data were acquired using a spectrograph (Spex 270M) and a photodiode array (Hamamatsu HC233–0900 with a NMOS C9564 array) as

described previously.[23,92] Spectra were chirp corrected and analyzed using Surface Xplorer software and plotted using Igor Pro.

Nanosecond, variable-temperature time-resolved absorption measurements were carried out using an Opotek Vibrant 355 LD Q-switched Nd:YAG laser pumping an Opotek optical parametric oscillator coupled to an Edinburgh Instruments LP980 spectrometer fitted with a Hamamatsu R928 photomultiplier tube and interfaced to a Tektronix TDS 3032C oscilloscope. Samples were dissolved in either spectral grade CH_3CN or dried and distilled THF, deoxygenated via at least 3 freeze-pump-thaw cycles prior to all measurements, and placed in an air-tight 1 cm quartz cuvette with an absorbance in the range of 0.4 – 0.7 at the excitation wavelength. The temperature was controlled using a TC 1 Temperature Controller from Quantum Northwest. The data were collected in 5 K increments, with a high temperature of 273 K and a low temperature of 223 K (THF) or 243 K (CH_3CN). All data were plotted in Igor Pro and fitted using a Gaussian deconvolution of the data to account for the instrument response function of the spectrometer (~5 ns). The sample was excited at 480 nm and probed at 460 nm. All experiments were carried out at least 3 separate times, with the data averaged between the runs. The error in the lifetime was determined from the fit, added to and subtracted from the lifetime of that run to get the lower and higher limits, and then the standard deviation between the experiments was taken to give the error. Following all experiments, a UV-Vis was taken of the sample and compared to an absorbance spectrum taken before to confirm the sample integrity.

Computational Details: All computational work was carried out using Orca v.5.0.2.[93–95] DFT optimizations were done at the O3LYP/def2SVP[96,97] level of theory, using the SMD[98] solvent

model (CH_3CN) and Grimme's D4 dispersion correction.[99,100] The following convergence criteria was used during optimization (verytightopt, tightscf). A frequency calculation was performed on all optimizations to confirm the optimized geometries were at a minimum. The lowest energy triplet and quintet states were calculated using the same method. TD-DFT was performed with various functionals and compared to the absorbance spectrum accuracy. O3LYP[96] and TPPSh[101,102] were found to be the best and single point calculations were performed at the both these levels of theory,[96] with O3LYP being the most accurate and used in discussion. def2-TZVP[97] basis set was applied to all atoms and also incorporated was the SMD[98] solvent model (CH_3CN, THF), the resolution of identity approximation (RIJCOSX)[103] to speed up the calculations, with the def2/J auxiliary basis set.[104] SCF convergence was set to TightSCF. For single point calculations Grimme's D4 dispersion correction[99,100] was also included. TD-DFT was done with and without D4 correction and no difference was observed in the resulting spectrum or excited states. Molecular orbital analyses were carried out using the Hirshfeld partition method[105] available in Multiwfn software.[106] Avagadro[107] was employed to visualize the molecular orbitals. The results of TD-DFT were analyzed and cube files for electron-hole maps were generated,[108] using Multiwfn.[106] Spin density maps, electron-hole figures and singly occupied molecular orbitals were printed out using Gabedit.[109] To calculate ground-state, excited state, driving force and reorganization energies, the following, previously established, protocol was followed: (1) The GS geometry was first optimized by restricted DFT (charge = 2, multiplicity = 1) using the crystal structure coordinates as starting input. The results were compared to the crystal structure to verify the accuracy of the level of theory. Using this verified method, the ^{3}MC (charge = 2, multiplicity = 3) and ^{5}MC (charge = 2, multiplicity = 5) geometries were optimized with unrestricted DFT using the optimized GS geometry as starting input. Frequency calculations were carried out with

each optimization to confirm that these structures are at a minimum. (2) TD-DFT was then carried out with charge = 2, and multiplicity = 1. Population analysis was performed to determine the relative molecular fragment contributions to the frontier MOs which contribute to the electronic transitions. (3) Single point calculations were then done, and the relative energies from the ground-state were calculated using the resulting energies. (4) For the theoretical driving force, the energy difference between single point calculations from the ^{3}MC optimized geometry and GS optimized geometry was used, with zero-point corrections were included from the optimization. For reorganizational energy zero-point corrections were also included and it was calculated as the energy difference between the ^{3}MC spin at the ^{3}MC optimized geometry and the ^{3}MC state at the ground state geometry. Due to the fact that we were unable to benchmark the MC excited state energies with experimental data the SP calculations for driving force were repeated with a range of Hartree-Fock exchange applied to the O3LYP functional (0%-30% in 5% increments and 40%), to prove that the conclusions are consistent with the traditional O3LYP (HF = 12 %) and independent of the computational results. To further support the idea that the experimental conclusions are independent of the computational results SP calculations were also done to compare the driving force with 4 different functionals: TPSSh, O3LYP, B3LYP,[110–112] and PBE0[113,114] which all gave results consistent with a ^{3}MC state.

X-Ray Crystallography: X-ray crystal structure data was collected from multi-faceted crystals of suitable size and quality selected from a representative sample of crystals of the same habit using an optical microscope. In each case, crystals were mounted on MiTiGen loops and data collection carried out in a cold stream of nitrogen (150 K; Bruker D8 QUEST ECO; Mo Kα radiation). All diffractometer manipulations were carried out using Bruker APEX3 software. Structure solution

and refinement was carried out using XS, XT and XL software, embedded 40 within the Bruker SHELXTL suite. For each structure, the absence of additional symmetry was confirmed using ADDSYM incorporated in the PLATON program. CCDC deposition numbers 2383378-2383379 contain the supplementary crystallographic data for this paper which can be obtained free of charge via https://www.ccdc.cam.ac.uk/.

Crystal structure parameters for [**L**H]PF_6 (CCDC 2383379): X-ray quality crystals were grown from a layered diffusion of chloroform and hexanes. Yellow blocks $C_{47}H_{37}Cl_3F_{12}N_6P_2$ 1082.11 g/mol, monoclinic, space group $P2_1/c$; a = 11.450(3) Å, b = 8.0459(15) Å, c = 48.980(12) Å, α = γ = 90°, β = 90.040(17)°; V = 4512.4(17) Å^3; Z = 4, ρ_{calcd} = 1.593 g cm^{-3}; crystal dimensions 0.150 x 0.110 x 0.080 mm; $2\theta_{max}$ = 49.824°; 87430 reflections, 7843 independent (R_{int} = 0.1005), intrinsic phasing; absorption coeff (μ = 0.368 mm^{-1}), absorption correction semi-empirical from equivalents (SADABS); refinement (against F_o^2) with SHELXTL V6.1, 633 parameters, 0 restraints, R_1 = 0.0936 ($I > 2\sigma$) and wR_2 = 0.2112 (all data), Goof = 1.103, residual electron density 1.14/−0.67 Å^{-3}.

Crystal structure parameters for [(**L**)$_3$Fe][PF_6]$_2$ (CCDC 2383378): X-ray quality crystals were grown from a layered diffusion of acetonitrile and diethyl ether. Red blocks; $C_{284}H_{216}F_{48}N_{40}P_8Fe_4$ 5572.11 g/mol, monoclinic, space group $P2_1/n$; a = 13.9195(14) Å, b = 22.394(2) Å, c = 21.257(2) Å, α = γ = 90°, β = 107.0650(10)°; V = 6334.5(11) Å^3; Z = 1, ρ_{calcd} = 1.461 g cm^{-3}; crystal dimensions 0.409 x 0.262 x 0.199 mm; $2\theta_{max}$ = 53.156°; 71688 reflections, 13198 independent (R_{int} = 0.0512), intrinsic phasing; absorption coeff (μ = 0.377 mm^{-1}), absorption correction semi-empirical from equivalents (SADABS); refinement (against F_o^2) with SHELXTL V6.1, 869

parameters, 0 restraints, R_1 = 0.0546 ($I > 2\sigma$) and wR_2 = 0.1682 (all data), Goof = 1.029, residual electron density 0.66/−0.52 $Å^{-3}$.

ASSOCIATED CONTENT

Supporting Information. Supplementary figures including multi-nuclear NMR, HR-MS spectra for all compounds, additional X-ray figures and tables, supporting figures and tables for optical characterization including TA spectroscopy; description of transient absorption spectroscopy and computational methodology including data tables, figures, and coordinates. CCDC 2383379 and 2383378 contain the supplementary crystallographic data for this paper which can be obtained free of charge from the Cambridge Crystallographic Data Center via www.ccdc.cam.ac.uk/structures. The following files are available free of charge:

Supporting Information File (PDF)

Crystallographic Information Files (CIF)

AUTHOR INFORMATION

Corresponding Authors

David E. Herbert (david.herbert@umanitoba.ca)

James K. McCusker (jkm@chemistry.msu.edu)

ORCIDs

Robert J. Ortiz: 0000-0001-9078-765X

Rajarshi Mondal: 0000-0002-6819-6690

James K. McCusker: 0000-0002-5684-3117

David E. Herbert: 0000-0001-8190-2468

Author Contributions

All authors have given approval to the final version of the manuscript.

Conflicts of Interest

There are no conflicts of interest to declare.

ACKNOWLEDGEMENTS

We are grateful to Atanu Ghosh, Hayden Beissel and Bekah Bowers for assistance with TA measurements and helpful discussions. Support for this work came from the Natural Sciences Engineering Research Council of Canada (RGPIN-2022-04501 to DEH, CGS-D and the Michael Smith Foreign Study Supplement scholarship support to RJO), the Canadian Foundation for Innovation and Research Manitoba for an award in support of an X-ray diffractometer (CFI #32146), Compute Canada, and the Solar Photochemistry Program of the Chemical Sciences, Geosciences, and Biosciences Division, Office of Basic Energy Sciences, Office of Science, U.S. Department of Energy under grant no. DE-FG02-01ER15282 (JKM). We thank Dr. Michael J. Ferguson (University of Alberta, X-ray Crystallography Laboratory) for collection of XRD data from $[(\mathbf{L})_3Fe][PF_6]_2$.

REFERENCES

(1) Ciamician, G. Photochemistry of the Future. *Science* **1912**, *36*, 385–394.
(2) Lewis, N. S.; Nocera, D. G. Powering the Planet: Chemical Challenges in Solar Energy Utilization. *Proc. Natl. Acad. Sci.* **2006**, *103*, 15729–15735.
(3) Horváth, I. T. Introduction: Sustainable Chemistry. *Chem. Rev.* **2018**, *118*, 369–371.
(4) Prier, C. K.; Rankic, D. A.; MacMillan, D. W. C. Visible Light Photoredox Catalysis with Transition Metal Complexes: Applications in Organic Synthesis. *Chem. Rev.* **2013**, *113*, 5322–5363.
(5) Sutin, N.; Creutz, C. Light Induced Electron Transfer Reactions of Metal Complexes. *Pure Appl. Chem.* **1980**, *52*, 2717.
(6) Graedel, T. E.; Harper, E. M.; Nassar, N. T.; Nuss, P.; Reck, B. K. Criticality of Metals and Metalloids. *Proc. Natl. Acad. Sci.* **2015**, *112*, 4257–4262.
(7) Flamigni, L.; Barbieri, A.; Sabatini, C.; Ventura, B.; Barigelletti, F. Photochemistry and Photophysics of Coordination Compounds: Iridium. In *Photochemistry and Photophysics of Coordination Compounds II*; Balzani, V., Campagna, S., Eds.; Topics in Current Chemistry; Springer: Berlin, Heidelberg, 2007; pp 143–203.
(8) Wenger, O. S. Photoactive Complexes with Earth-Abundant Metals. *J. Am. Chem. Soc.* **2018**, *140*, 13522–13533.
(9) Büldt, L. A.; Guo, X.; Vogel, R.; Prescimone, A.; Wenger, O. S. A Tris(Diisocyanide)Chromium(0) Complex Is a Luminescent Analog of Fe(2,2′-Bipyridine)$_3^{2+}$. *J. Am. Chem. Soc.* **2017**, *139*, 985–992.
(10) Büldt, L. A.; Wenger, O. S. Chromium(0), Molybdenum(0), and Tungsten(0) Isocyanide Complexes as Luminophores and Photosensitizers with Long-Lived Excited States. *Angew. Chem. Int. Ed.* **2017**, *56*, 5676–5682.
(11) Sinha, N.; Wegeberg, C.; Häussinger, D.; Prescimone, A.; Wenger, O. S. Photoredox-Active Cr(0) Luminophores Featuring Photophysical Properties Competitive with Ru(II) and Os(II) Complexes. *Nat. Chem.* **2023**, *15*, 1730–1736.
(12) Wegeberg, C.; Wenger, O. S. Luminescent Chromium(0) and Manganese(I) Complexes. *Dalton Trans.* **2022**, *51*, 1297–1302.
(13) Herr, P.; Kerzig, C.; Larsen, C. B.; Häussinger, D.; Wenger, O. S. Manganese(I) Complexes with Metal-to-Ligand Charge Transfer Luminescence and Photoreactivity. *Nat. Chem.* **2021**, *13*, 956–962.
(14) de Groot, L. H. M.; Ilic, A.; Schwarz, J.; Wärnmark, K. Iron Photoredox Catalysis–Past, Present, and Future. *J. Am. Chem. Soc.* **2023**, *145*, 9369–9388.
(15) McCusker, J. K. Electronic Structure in the Transition Metal Block and Its Implications for Light Harvesting. *Science* **2019**, *363*, 484–488.
(16) Woodhouse, M. D.; McCusker, J. K. Mechanistic Origin of Photoredox Catalysis Involving Iron(II) Polypyridyl Chromophores. *J. Am. Chem. Soc.* **2020**, *142*, 16229–16233.
(17) Kaufhold, S.; Rosemann, N. W.; Chábera, P.; Lindh, L.; Bolaño Losada, I.; Uhlig, J.; Pascher, T.; Strand, D.; Wärnmark, K.; Yartsev, A.; Persson, P. Microsecond Photoluminescence and Photoreactivity of a Metal-Centered Excited State in a Hexacarbene–Co(III) Complex. *J. Am. Chem. Soc.* **2021**, *143*, 1307–1312.
(18) Alowakennu, M. M.; Ghosh, A.; McCusker, J. K. Direct Evidence for Excited Ligand Field State-Based Oxidative Photoredox Chemistry of a Cobalt(III) Polypyridyl Photosensitizer. *J. Am. Chem. Soc.* **2023**, *145*, 20786–20791.

(19) Chan, A. Y.; Ghosh, A.; Yarranton, J. T.; Twilton, J.; Jin, J.; Arias-Rotondo, D. M.; Sakai, H. A.; McCusker, J. K.; MacMillan, D. W. C. Exploiting the Marcus Inverted Region for First-Row Transition Metal–Based Photoredox Catalysis. *Science* **2023**, *382*, 191–197.
(20) Wasielewski, M. R.; Forbes, M. D. E.; Frank, N. L.; Kowalski, K.; Scholes, G. D.; Yuen-Zhou, J.; Baldo, M. A.; Freedman, D. E.; Goldsmith, R. H.; Goodson, T.; Kirk, M. L.; McCusker, J. K.; Ogilvie, J. P.; Shultz, D. A.; Stoll, S.; Whaley, K. B. Exploiting Chemistry and Molecular Systems for Quantum Information Science. *Nat. Rev. Chem.* **2020**, *4*, 490–504.
(21) Creutz, C.; Chou, M.; Netzel, T. L.; Okumura, M.; Sutin, N. Lifetimes, Spectra, and Quenching of the Excited States of Polypyridine Complexes of Iron(II), Ruthenium(II), and Osmium(II). *J. Am. Chem. Soc.* **1980**, *102*, 1309–1319.
(22) McCusker, J. K.; Walda, K. N.; Dunn, R. C.; Simon, J. D.; Magde, D.; Hendrickson, D. N. Subpicosecond ^{1}MLCT→$^{5}T_2$ Intersystem Crossing of Low-Spin Polypyridyl Ferrous Complexes. *J. Am. Chem. Soc.* **1993**, *115*, 298–307.
(23) Paulus, B. C.; Nielsen, K. C.; Tichnell, C. R.; Carey, M. C.; McCusker, J. K. A Modular Approach to Light Capture and Synthetic Tuning of the Excited-State Properties of Fe(II)-Based Chromophores. *J. Am. Chem. Soc.* **2021**, *143*, 8086–8098.
(24) Kjær, K. S.; Kunnus, K.; Harlang, T. C. B.; Driel, T. B. V.; Ledbetter, K.; Hartsock, R. W.; Reinhard, M. E.; Koroidov, S.; Li, L.; Laursen, M. G.; Biasin, E.; Hansen, F. B.; Vester, P.; Christensen, M.; Haldrup, K.; Nielsen, M. M.; Chabera, P.; Liu, Y.; Tatsuno, H.; Timm, C.; Uhlig, J.; Sundstöm, V.; Németh, Z.; Szemes, D. S.; Bajnóczi, É.; Vankó, G.; Alonso-Mori, R.; Glownia, J. M.; Nelson, S.; Sikorski, M.; Sokaras, D.; Lemke, H. T.; Canton, S. E.; Wärnmark, K.; Persson, P.; Cordones, A. A.; Gaffney, K. J. Solvent Control of Charge Transfer Excited State Relaxation Pathways in [Fe(2,2′-Bipyridine)$(CN)_4$]$^{2-}$. *Phys. Chem. Chem. Phys.* **2018**, *20*, 4238–4249.
(25) Steube, J.; Burkhardt, L.; Päpcke, A.; Moll, J.; Zimmer, P.; Schoch, R.; Wölper, C.; Heinze, K.; Lochbrunner, S.; Bauer, M. Excited-State Kinetics of an Air-Stable Cyclometalated Iron(II) Complex. *Chem. Eur. J.* **2019**, *25*, 11826–11830.
(26) Witas, K.; Nair, S. S.; Maisuradze, T.; Zedler, L.; Schmidt, H.; Garcia-Porta, P.; Rein, A. S. J.; Bolter, T.; Rau, S.; Kupfer, S.; Dietzek-Ivanšić, B.; Sorsche, D. U. Beyond the First Coordination Sphere─Manipulating the Excited-State Landscape in Iron(II) Chromophores with Protons. *J. Am. Chem. Soc.* **2024**, *146*, 19710–19719.
(27) Zhang, W.; Alonso-Mori, R.; Bergmann, U.; Bressler, C.; Chollet, M.; Galler, A.; Gawelda, W.; Hadt, R. G.; Hartsock, R. W.; Kroll, T.; Kjaer, K. S.; Kubicek, K.; Lemke, H. T.; Liang, H. W.; Meyer, D. A.; Nielsen, M. M.; Purser, C.; Robinson, J. S.; Solomon, E. I.; Sun, Z.; Sokaras, D.; van Driel, T. B.; Vanko, G.; Weng, T.-C.; Zhu, D.; Gaffney, K. J. Tracking Excited-State Charge and Spin Dynamics in Iron Coordination Complexes. *Nature* **2014**, *509*, 345–348.
(28) Winkler, J. R.; Creutz, C.; Sutin, N. Solvent Tuning of the Excited-State Properties of (2,2'-Bipyridine)Tetracyanoferrate(II): Direct Observation of a Metal-to-Ligand Charge-Transfer Excited State of Iron(II). *J. Am. Chem. Soc.* **1987**, *109*, 3470–3471.
(29) Winkler, J. R.; Sutin, N. Lifetimes and Spectra of the Excited States of Cis-Dicyanobis(2,2'-Bipyridine)Iron(II) and -Ruthenium(II) in Solution. *Inorg. Chem.* **1987**, *26*, 220–221.

(30) Ferrere, S. New Photosensitizers Based upon $[Fe(L)_2(CN)_2]$ and $[Fe(L)_3]$ (L = Substituted 2,2'-Bipyridine): Yields for the Photosensitization of TiO_2 and Effects on the Band Selectivity. *Chem. Mater.* **2000**, *12*, 1083–1089.
(31) Zhang, W.; Kjær, K. S.; Alonso-Mori, R.; Bergmann, U.; Chollet, M.; Fredin, L. A.; Hadt, R. G.; Hartsock, R. W.; Harlang, T.; Kroll, T.; Kubiček, K.; Lemke, H. T.; Liang, H. W.; Liu, Y.; Nielsen, M. M.; Persson, P.; Robinson, J. S.; Solomon, E. I.; Sun, Z.; Sokaras, D.; van Driel, T. B.; Weng, T.-C.; Zhu, D.; Wärnmark, K.; Sundström, V.; Gaffney, K. J. Manipulating Charge Transfer Excited State Relaxation and Spin Crossover in Iron Coordination Complexes with Ligand Substitution. *Chem. Sci.* **2017**, *8*, 515–523.
(32) Vittardi, S. B.; Magar, R. T.; Schrage, B. R.; Ziegler, C. J.; Jakubikova, E.; Rack, J. J. Evidence for a Lowest Energy ^{3}MLCT Excited State in $[Fe(tpy)(CN)_3]^-$. *Chem. Commun.* **2021**, 4658–4661.
(33) Dixon, I. M.; Alary, F.; Boggio-Pasqua, M.; Heully, J.-L. Reversing the Relative ^{3}MLCT–^{3}MC Order in Fe(II) Complexes Using Cyclometallating Ligands: A Computational Study Aiming at Luminescent Fe(II) Complexes. *Dalton Trans.* **2015**, *44*, 13498–13503.
(34) Leis, W.; Argüello Cordero, M. A.; Lochbrunner, S.; Schubert, H.; Berkefeld, A. A Photoreactive Iron(II) Complex Luminophore. *J. Am. Chem. Soc.* **2022**, *144*, 1169–1173.
(35) Liu, Y.; Warnmark, K.; Liu, Y.; Sundstrom, V.; Persson, P. Fe N-Heterocyclic Carbene Complexes as Promising Photosensitizers. *Acc. Chem. Res* **2016**, *49*, 1477–1485.
(36) Reuter, T.; Kruse, A.; Schoch, R.; Lochbrunner, S.; Bauer, M.; Heinze, K. Higher MLCT Lifetime of Carbene Iron(II) Complexes by Chelate Ring Expansion. *Chem. Commun.* **2021**, *57*, 7541–7544.
(37) Sinha, N.; Pfund, B.; Wegeberg, C.; Prescimone, A.; Wenger, O. S. Cobalt(III) Carbene Complex with an Electronic Excited-State Structure Similar to Cyclometalated Iridium(III) Compounds. *J. Am. Chem. Soc.* **2022**, *144*, 9859–9873.
(38) Malme, J. T.; Clendening, R. A.; Ash, R.; Curry, T.; Ren, T.; Vura-Weis, J. Nanosecond Metal-to-Ligand Charge-Transfer State in an Fe(II) Chromophore: Lifetime Enhancement via Nested Potentials. *J. Am. Chem. Soc.* **2023**, *145*, 6029–6034.
(39) Liu, Y.; Kjær, K. S.; Fredin, L. A.; Chábera, P.; Harlang, T.; Canton, S. E.; Lidin, S.; Zhang, J.; Lomoth, R.; Bergquist, K.-E.; Persson, P.; Wärnmark, K.; Sundström, V. A Heteroleptic Ferrous Complex with Mesoionic Bis(1,2,3-Triazol-5-Ylidene) Ligands: Taming the MLCT Excited State of Iron(II). *Chem. Eur. J.* **2015**, *21*, 3628–3639.
(40) Liu, Y.; Persson, P.; Sundström, V.; Wärnmark, K. Fe N-Heterocyclic Carbene Complexes as Promising Photosensitizers. *Acc. Chem. Res.* **2016**, *49*, 1477–1485.
(41) Chábera, P.; Kjaer, K. S.; Prakash, O.; Honarfar, A.; Liu, Y.; Fredin, L. A.; Harlang, T. C. B.; Lidin, S.; Uhlig, J.; Sundström, V.; Lomoth, R.; Persson, P.; Wärnmark, K. FeII Hexa N-Heterocyclic Carbene Complex with a 528 Ps Metal-to-Ligand Charge-Transfer Excited-State Lifetime. *J. Phys. Chem. Lett.* **2018**, *9*, 459–463.
(42) Magra, K.; Darari, M.; Domenichini, E.; Francés-Monerris, A.; Cebrián, C.; Beley, M.; Pastore, M.; Monari, A.; Assfeld, X.; Haacke, S.; Gros, P. C. Photophysical Investigation of Iron(II) Complexes Bearing Bidentate Annulated Isomeric Pyridine-NHC Ligands. *J. Phys. Chem. C* **2020**, *124*, 18379–18389.
(43) Magra, K.; Domenichini, E.; Francés-Monerris, A.; Cebrián, C.; Beley, M.; Darari, M.; Pastore, M.; Monari, A.; Assfeld, X.; Haacke, S.; Gros, P. C. Impact of the Fac/Mer Isomerism on the Excited-State Dynamics of Pyridyl-Carbene Fe(II) Complexes. *Inorg. Chem.* **2019**, *58*, 5069–5081.

(44) Magra, K.; Francés-Monerris, A.; Cebrián, C.; Monari, A.; Haacke, S.; Gros, P. C. Bidentate Pyridyl-NHC Ligands: Synthesis, Ground and Excited State Properties of Their Iron(II) Complexes and the Role of the Fac/Mer Isomerism. *Eur. J. Inorg. Chem.* **2022**, e202100818.
(45) Dierks, P.; Vukadinovic, Y.; Bauer, M. Photoactive Iron Complexes: More Sustainable, but Still a Challenge. *Inorg. Chem. Front.* **2022**, *9*, 206–220.
(46) Paulus, B. C.; Adelman, S. L.; Jamula, L. L.; McCusker, J. K. Leveraging Excited-State Coherence for Synthetic Control of Ultrafast Dynamics. *Nature* **2020**, *582*, 214–218.
(47) Herbert, D. E. When Is a Pyridine Not a Pyridine? Benzannulated *N* -Heterocyclic Ligands in Molecular Materials Chemistry. *Can. J. Chem.* **2023**, *101*, 892–902.
(48) Mandapati, P.; Braun, J. D.; Lozada, I. B.; Williams, J. A. G.; Herbert, D. E. Deep-Red Luminescence from Platinum(II) Complexes of N^N–^N-Amido Ligands with Benzannulated N-Heterocyclic Donor Arms. *Inorg. Chem.* **2020**, *59*, 12504–12517.
(49) Mandapati, P.; Braun, J. D.; Killeen, C.; Davis, R. L.; Williams, J. A. G.; Herbert, D. E. Luminescent Platinum(II) Complexes of N^N–^N Amido Ligands with Benzannulated N-Heterocyclic Donor Arms: Quinolines Offer Unexpectedly Deeper Red Phosphorescence than Phenanthridines. *Inorg. Chem.* **2019**, *58*, 14808–14817.
(50) Ortiz, R. J.; Braun, J. D.; Williams, J. A. G.; Herbert, D. E. Brightly Luminescent Platinum Complexes of N^C–^N Ligands Forming Six-Membered Chelate Rings: Offsetting Deleterious Ring Size Effects Using Site-Selective Benzannulation. *Inorg. Chem.* **2021**, *60*, 16881–16894.
(51) Braun, J. D.; Lozada, I. B.; Kolodziej, C.; Burda, C.; Newman, K. M. E.; van Lierop, J.; Davis, R. L.; Herbert, D. E. Iron(II) Coordination Complexes with Panchromatic Absorption and Nanosecond Charge-Transfer Excited State Lifetimes. *Nat. Chem.* **2019**, *11*, 1144–1150.
(52) Mondal, R.; Ortiz, R. J.; Braun, J. D.; Herbert, D. E. Synthesis, Characterization, and Coordination Chemistry of a Phenanthridine-Containing N-Heterocyclic Carbene Ligand. *Can. J. Chem.* **2021**, *99*, 245–252.
(53) Carrillo, U.; Francés-Monerris, A.; Marri, A. R.; Cebrián, C.; Gros, P. C. Substituent-Induced Control of Fac/Mer Isomerism in Azine-NHC Fe(II) Complexes. *ACS Org. Inorg. Au* **2022**, *2*, 525–536.
(54) Mondal, R.; Braun, J. D.; Lozada, I. B.; Nickel, R.; van Lierop, J.; Herbert, D. E. Group VIII Coordination Complexes of Bidentate P^N Ligands Bearing π-Extended Quinoline or Phenanthridine N-Heterocycles. *New J. Chem.* **2021**, *45*, 4427–4436.
(55) Parenti, F.; Tassinari, F.; Libertini, E.; Lanzi, M.; Mucci, A. Π-Stacking Signature in NMR Solution Spectra of Thiophene-Based Conjugated Polymers. *ACS Omega* **2017**, *2*, 5775–5784.
(56) Mandapati, P.; Giesbrecht, P. K.; Davis, R. L.; Herbert, D. E. Phenanthridine-Containing Pincer-like Amido Complexes of Nickel, Palladium, and Platinum. *Inorg. Chem.* **2017**, *56*, 3674–3685.
(57) Manuta, D. M.; Lees, A. J. Solvatochromism of the Metal to Ligand Charge-Transfer Transitions of Zerovalent Tungsten Carbonyl Complexes. *Inorg. Chem.* **1986**, *25*, 3212–3218.
(58) Chábera, P.; Liu, Y.; Prakash, O.; Thyrhaug, E.; Nahhas, A. E.; Honarfar, A.; Essén, S.; Fredin, L. A.; Harlang, T. C. B.; Kjær, K. S.; Handrup, K.; Ericson, F.; Tatsuno, H.; Morgan, K.; Schnadt, J.; Häggström, L.; Ericsson, T.; Sobkowiak, A.; Lidin, S.; Huang,

P.; Styring, S.; Uhlig, J.; Bendix, J.; Lomoth, R.; Sundström, V.; Persson, P.; Wärnmark, K. A Low-Spin Fe(III) Complex With 100-Ps Ligand-to-Metal Charge Transfer Photoluminescence. *Nature* **2017**, *543*, 695.

(59) Heath, G. A.; Yellowlees, L. J.; Braterman, P. S. Spectro-Electrochemical Studies on Tris-Bipyridyl Ruthenium Complexes; Ultra-Violet, Visible, and near-Infrared Spectra of the Series $[Ru(Bipyridyl)_3]^{2+/1+/0/1-}$. *J. Chem. Soc., Chem. Commun.* **1981**, No. 6, 287–289.

(60) Brown, A. M.; McCusker, C. E.; McCusker, J. K. Spectroelectrochemical Identification of Charge-Transfer Excited States in Transition Metal-Based Polypyridyl Complexes. *Dalton Trans.* **2014**, *43*, 17635–17646.

(61) Constable, E. C.; Baum, G.; Bill, E.; Dyson, R.; van Eldik, R.; Fenske, D.; Kaderli, S.; Morris, D.; Neubrand, A.; Neuburger, M.; Smith, D. R.; Wieghardt, K.; Zehnder, M.; Zuberbühler, A. D. Control of Iron(II) Spin States in 2,2′:6′,2″-Terpyridine Complexes through Ligand Substitution. *Chem. - Eur. J.* **1999**, *5*, 498–508.

(62) Cebrián, C.; Pastore, M.; Monari, A.; Assfeld, X.; Gros, P. C.; Haacke, S. Ultrafast Spectroscopy of Fe(II) Complexes Designed for Solar-Energy Conversion: Current Status and Open Questions. *ChemPhysChem* **2022**, *23*, e202100659.

(63) Ghosh, A.; Yarranton, J. T.; McCusker, J. K. Establishing the Origin of Marcus-Inverted-Region Behaviour in the Excited-State Dynamics of Cobalt(III) Polypyridyl Complexes. *Nat. Chem.* **2024**, *16*, 1665–1672.

(64) Tatsuno, H.; Kjær, K. S.; Kunnus, K.; Harlang, T. C. B.; Timm, C.; Guo, M.; Chàbera, P.; Fredin, L. A.; Hartsock, R. W.; Reinhard, M. E.; Koroidov, S.; Li, L.; Cordones, A. A.; Gordivska, O.; Prakash, O.; Liu, Y.; Laursen, M. G.; Biasin, E.; Hansen, F. B.; Vester, P.; Christensen, M.; Haldrup, K.; Németh, Z.; Sárosiné Szemes, D.; Bajnóczi, É.; Vankó, G.; Van Driel, T. B.; Alonso-Mori, R.; Glownia, J. M.; Nelson, S.; Sikorski, M.; Lemke, H. T.; Sokaras, D.; Canton, S. E.; Dohn, A. O.; Møller, K. B.; Nielsen, M. M.; Gaffney, K. J.; Wärnmark, K.; Sundström, V.; Persson, P.; Uhlig, J. Hot Branching Dynamics in a Light-Harvesting Iron Carbene Complex Revealed by Ultrafast X-Ray Emission Spectroscopy. *Angew. Chem. Int. Ed.* **2020**, *59*, 364–372.

(65) Kunnus, K.; Vacher, M.; Harlang, T. C. B.; Kjær, K. S.; Haldrup, K.; Biasin, E.; van Driel, T. B.; Pápai, M.; Chabera, P.; Liu, Y.; Tatsuno, H.; Timm, C.; Källman, E.; Delcey, M.; Hartsock, R. W.; Reinhard, M. E.; Koroidov, S.; Laursen, M. G.; Hansen, F. B.; Vester, P.; Christensen, M.; Sandberg, L.; Németh, Z.; Szemes, D. S.; Bajnóczi, É.; Alonso-Mori, R.; Glownia, J. M.; Nelson, S.; Sikorski, M.; Sokaras, D.; Lemke, H. T.; Canton, S. E.; Møller, K. B.; Nielsen, M. M.; Vankó, G.; Wärnmark, K.; Sundström, V.; Persson, P.; Lundberg, M.; Uhlig, J.; Gaffney, K. J. Vibrational Wavepacket Dynamics in Fe Carbene Photosensitizer Determined with Femtosecond X-Ray Emission and Scattering. *Nat. Commun.* **2020**, *11*, 634.

(66) Carey, M. C.; Adelman, S. L.; McCusker, J. K. Insights into the Excited State Dynamics of Fe(II) Polypyridyl Complexes from Variable-Temperature Ultrafast Spectroscopy. *Chem. Sci.* **2019**, *10*, 134–144.

(67) Reuter, T.; Zorn, D.; Naumann, R.; Klett, J.; Förster, C.; Heinze, K. A Tetracarbene Iron(II) Complex with a Long-Lived Triplet Metal-to-Ligand Charge Transfer State Due to a Triplet-Triplet Barrier. *Angew. Chem. Int. Ed.* **2024**, 63, e202406438

(68) Lindh, L.; Pascher, T.; Persson, S.; Goriya, Y.; Wärnmark, K.; Uhlig, J.; Chábera, P.; Persson, P.; Yartsev, A. Multifaceted Deactivation Dynamics of Fe(II) N-Heterocyclic Carbene Photosensitizers. *J. Phys. Chem. A* **2023**, *127*, 10210–10222.

(69) McCusker, J. K.; Rheingold, A. L.; Hendrickson, D. N. Variable-Temperature Studies of Laser-Initiated $^5T_2 \rightarrow {}^1A_1$ Intersystem Crossing in Spin-Crossover Complexes: Empirical Correlations between Activation Parameters and Ligand Structure in a Series of Polypyridyl Ferrous Complexes. *Inorg. Chem.* **1996**, *35*, 2100–2112.
(70) McGarvey, J. J.; Lawthers, I.; Heremans, K.; Toftlund, H. Kinetics of Spin-State Interconversion in Iron(II) Complexes in Solution as a Function of Pressure: Activation Volumes for the $^1A_1 \leftrightharpoons {}^5T_2$ Spin Change. *Inorg. Chem.* **1990**, *29*, 252–256.
(71) Al-Obaidi, A. H. R.; Jensen, K. B.; McGarvey, J. J.; Toftlund, H.; Jensen, B.; Bell, S. E. J.; Carroll, J. G. Structural and Kinetic Studies of Spin Crossover in an Iron(II) Complex with a Novel Tripodal Ligand. *Inorg. Chem.* **1996**, *35*, 5055–5060.
(72) Bowman, D. N.; Jakubikova, E. Low-Spin versus High-Spin Ground State in Pseudo-Octahedral Iron Complexes. *Inorganic Chemistry* **2012**, *51*, 6011–6019.
(73) Beissel, H. F. Characterizing Fe(II)-Polypyridine Excited State Evolution Using Transient Absorption Spectroscopy. PhD, Michigan State University, 2024.
(74) Tanabe, Y.; Sugano, S. On the Absorption Spectra of Complex Ions II. *J. Phys. Soc. Jpn.* **1954**, *9*, 766–779.
(75) Miller, J. N.; McCusker, J. K. Outer-Sphere Effects on Ligand-Field Excited-State Dynamics: Solvent Dependence of High-Spin to Low-Spin Conversion in [Fe(Bpy)3]2+. *Chem. Sci.* **2020**, *11*, 5191–5204.
(76) Pápai, M.; Vankó, G.; de Graaf, C.; Rozgonyi, T. Theoretical Investigation of the Electronic Structure of Fe(II) Complexes at Spin-State Transitions. *J. Chem. Theory Comput.* **2013**, *9*, 509–519.
(77) Sousa, C.; de Graaf, C.; Rudavskyi, A.; Broer, R.; Tatchen, J.; Etinski, M.; Marian, C. M. Ultrafast Deactivation Mechanism of the Excited Singlet in the Light-Induced Spin Crossover of $[Fe(2,2'\text{-Bipyridine})_3]^{2+}$. *Chem. - Eur. J.* **2013**, *19*, 17541–17551.
(78) He, L.; Ma, D.; Duan, L.; Wei, Y.; Qiao, J.; Zhang, D.; Dong, G.; Wang, L.; Qiu, Y. Control of Intramolecular π–π Stacking Interaction in Cationic Iridium Complexes via Fluorination of Pendant Phenyl Rings. *Inorg. Chem.* **2012**, *51*, 4502–4510.
(79) Costa, R. D.; Ortí, E.; Bolink, H. J.; Graber, S.; Housecroft, C. E.; Constable, E. C. Intramolecular π-Stacking in a Phenylpyrazole-Based Iridium Complex and Its Use in Light-Emitting Electrochemical Cells. *J. Am. Chem. Soc.* **2010**, *132*, 5978–5980.
(80) Poirot, A.; Vanucci-Bacqué, C.; Delavaux-Nicot, B.; Meslien, C.; Saffon-Merceron, N.; Serpentini, C.-L.; Bedos-Belval, F.; Benoist, E.; Fery-Forgues, S. Using a Diphenyl-Bi-(1,2,4-Triazole) Tricarbonylrhenium(I) Complex with Intramolecular π–π Stacking Interaction for Efficient Solid-State Luminescence Enhancement. *Dalton Trans.* **2023**, *52*, 5453–5465.
(81) Carter-Fenk, K.; Herbert, J. M. Reinterpreting π-Stacking. *Phys. Chem. Chem. Phys.* **2020**, *22*, 24870–24886.
(82) Martinez, C. R.; Iverson, B. L. Rethinking the Term "Pi-Stacking." *Chem. Sci.* **2012**, *3*, 2191–2201.
(83) Ashley, D. C.; Jakubikova, E. Ray-Dutt and Bailar Twists in Fe(II)-Tris(2,2'-Bipyridine): Spin States, Sterics, and Fe-N Bond Strengths. *Inorg. Chem.* **2018**, *57*, 5585–5596.
(84) Ketkaew, R.; Tantirungrotechai, Y.; Harding, P.; Chastanet, G.; Guionneau, P.; Marchivie, M.; Harding, D. J. OctaDist: A Tool for Calculating Distortion Parameters in Spin Crossover and Coordination Complexes. *Dalton Trans.* **2021**, *50*, 1086–1096.

(85) Britz, A.; Gawelda, W.; Assefa, T. A.; Jamula, L. L.; Yarranton, J. T.; Galler, A.; Khakhulin, D.; Diez, M.; Harder, M.; Doumy, G.; March, A. M.; Bajnóczi, É.; Németh, Z.; Pápai, M.; Rozsályi, E.; Sárosiné Szemes, D.; Cho, H.; Mukherjee, S.; Liu, C.; Kim, T. K.; Schoenlein, R. W.; Southworth, S. H.; Young, L.; Jakubikova, E.; Huse, N.; Vankó, G.; Bressler, C.; McCusker, J. K. Using Ultrafast X-Ray Spectroscopy To Address Questions in Ligand-Field Theory: The Excited State Spin and Structure of $[Fe(dcpp)_2]^{2+}$. *Inorg. Chem.* **2019**, *58*, 9341–9350.
(86) Reinhard, M. E.; Sidhu, B. K.; Lozada, I. B.; Powers-Riggs, N.; Ortiz, R. J.; Lim, H.; Nickel, R.; Lierop, J. van; Alonso-Mori, R.; Chollet, M.; Gee, L. B.; Kramer, P. L.; Kroll, T.; Raj, S. L.; van Driel, T. B.; Cordones, A. A.; Sokaras, D.; Herbert, D. E.; Gaffney, K. J. Time-Resolved X-Ray Emission Spectroscopy and Synthetic High-Spin Model Complexes Resolve Ambiguities in Excited-State Assignments of Transition-Metal Chromophores: A Case Study of Fe-Amido Complexes. *J. Am. Chem. Soc.* **2024**, *146*, 17908–17916.
(87) Gao, Y.; Cai, Z.; Li, S.; Li, G. Rhodium(I)-Catalyzed Aryl C–H Carboxylation of 2-Arylanilines with CO_2. *Org. Lett.* **2019**, *21*, 3663–3669.
(88) Zhao, Y.; Gilbertson, S. R. Synthesis of Proline-Based N-Heterocyclic Carbene Ligands. *Org. Lett.* **2014**, *16*, 1033–1035.
(89) Zhu, L.; Guo, P.; Li, G.; Lan, J.; Xie, R.; You, J. Simple Copper Salt-Catalyzed N-Arylation of Nitrogen-Containing Heterocycles with Aryl and Heteroaryl Halides. *J. Org. Chem.* **2007**, *72*, 8535–8538.
(90) Krejčik, M.; Daněk, M.; Hartl, F. Simple Construction of an Infrared Optically Transparent Thin-Layer Electrochemical Cell: Applications to the Redox Reactions of Ferrocene, $Mn_2(CO)_{10}$ and $Mn(CO)_3$(3,5-Di-t-Butyl-Catecholate)$^-$. *J. Electroanal. Chem. Interf. Electrochem.* **1991**, *317*, 179–187.
(91) Damrauer, N. H.; McCusker, J. K. Ultrafast Dynamics in the Metal-to-Ligand Charge Transfer Excited-State Evolution of [Ru(4,4‘-Diphenyl-2,2‘-Bipyridine)3]2+. *J. Phys. Chem. A* **1999**, *103*, 8440–8446.
(92) Brown, A. M.; McCusker, C. E.; Carey, M. C.; Blanco-Rodríguez, A. M.; Towrie, M.; Clark, I. P.; Vlček, A.; McCusker, J. K. Vibrational Relaxation and Redistribution Dynamics in Ruthenium(II) Polypyridyl-Based Charge-Transfer Excited States: A Combined Ultrafast Electronic and Infrared Absorption Study. *J. Phys. Chem. A* **2018**, *122*, 7941–7953.
(93) Neese, F. The ORCA Program System. *WIREs Comput. Mol. Sci.* **2012**, *2*, 73–78.
(94) Neese, F. Software Update: The ORCA Program System—Version 5.0. *WIREs Comput. Mol. Sci.* **2022**, *12*, e1606.
(95) Neese, F.; Wennmohs, F.; Becker, U.; Riplinger, C. The ORCA Quantum Chemistry Program Package. *J. Chem. Phys.* **2020**, *152*, 224108.
(96) Cohen, A. J.; Handy, N. C. Dynamic Correlation. *Mol. Phys.* **2001**, *99*, 607–615.
(97) Weigend, F.; Ahlrichs, R. Balanced Basis Sets of Split Valence, Triple Zeta Valence and Quadruple Zeta Valence Quality for H to Rn: Design and Assessment of Accuracy. *Phys. Chem. Chem. Phys.* **2005**, *7*, 3297–3305.
(98) Marenich, A. V.; Cramer, C. J.; Truhlar, D. G. Universal Solvation Model Based on Solute Electron Density and on a Continuum Model of the Solvent Defined by the Bulk Dielectric Constant and Atomic Surface Tensions. *J. Phys. Chem. B* **2009**, *113*, 6378–6396.

(99) Caldeweyher, E.; Ehlert, S.; Hansen, A.; Neugebauer, H.; Spicher, S.; Bannwarth, C.; Grimme, S. A Generally Applicable Atomic-Charge Dependent London Dispersion Correction. *J. Chem. Phys.* **2019**, *150*, 154122.
(100) Caldeweyher, E.; Bannwarth, C.; Grimme, S. Extension of the D3 Dispersion Coefficient Model. *J. Chem. Phys.* **2017**, *147*, 034112.
(101) Staroverov, V. N.; Scuseria, G. E.; Tao, J.; Perdew, J. P. Comparative Assessment of a New Nonempirical Density Functional: Molecules and Hydrogen-Bonded Complexes. *J. Chem. Phys.* **2003**, *119*, 12129–12137.
(102) Tao, J.; Perdew, J. P.; Staroverov, V. N.; Scuseria, G. E. Climbing the Density Functional Ladder: Nonempirical Meta--Generalized Gradient Approximation Designed for Molecules and Solids. *Phys. Rev. Lett.* **2003**, *91*, 146401.
(103) Neese, F.; Wennmohs, F.; Hansen, A.; Becker, U. Efficient, Approximate and Parallel Hartree–Fock and Hybrid DFT Calculations. A 'Chain-of-Spheres' Algorithm for the Hartree–Fock Exchange. *Chem. Phys.* **2009**, *356*, 98–109.
(104) Weigend, F. Accurate Coulomb-Fitting Basis Sets for H to Rn. *Phys. Chem. Chem. Phys.* **2006**, *8*, 1057–1065.
(105) Hirshfeld, F. L. Bonded-Atom Fragments for Describing Molecular Charge Densities. *Theoret. Chim. Acta* **1977**, *44*, 129–138.
(106) Lu, T.; Chen, F. Multiwfn: A Multifunctional Wavefunction Analyzer. *J. Comput. Chem.* **2012**, *33*, 580–592.
(107) Hanwell, M. D.; Curtis, D. E.; Lonie, D. C.; Vandermeersch, T.; Zurek, E.; Hutchison, G. R. Avogadro: An Advanced Semantic Chemical Editor, Visualization, and Analysis Platform. *J. Cheminform.* **2012**, *4*, 1–17.
(108) Liu, Z.; Lu, T.; Chen, Q. An Sp-Hybridized All-Carboatomic Ring, Cyclo[18]Carbon: Electronic Structure, Electronic Spectrum, and Optical Nonlinearity. *Carbon* **2020**, *165*, 461–467.
(109) Allouche, A.-R. Gabedit—A Graphical User Interface for Computational Chemistry Softwares. *J. Comput. Chem.* **2011**, *32*, 174–182.
(110) Lee, C.; Yang, W.; Parr, R. G. Development of the Colle-Salvetti Correlation-Energy Formula into a Functional of the Electron Density. *Phys. Rev. B* **1988**, *37*, 785–789.
(111) Becke, A. D. A New Mixing of Hartree–Fock and Local Density-functional Theories. *J. Chem. Phys.* **1993**, *98*, 1372–1377.
(112) Becke, A. D. Density-functional Thermochemistry. III. The Role of Exact Exchange. *J. Chem. Phys.* **1993**, *98*, 5648–5652.
(113) Adamo, C.; Barone, V. Toward Reliable Density Functional Methods without Adjustable Parameters: The PBE0 Model. *J. Chem. Phys.* **1999**, *110*, 6158–6170.
(114) Ernzerhof, M.; Scuseria, G. E. Assessment of the Perdew–Burke–Ernzerhof Exchange-Correlation Functional. *J. Chem. Phys.* **1999**, *110*, 5029–5036.

For Table of Contents Only